



Intra-Annual Rossby Waves Destabilization as a Potential Driver of Low-Latitude Zonal Jets: Barotropic Dynamics

AUDREY DELPECH,^a CLAIRE MÉNESGUEN,^b YVES MOREL,^a LEIF N. THOMAS,^c FRÉDÉRIC MARIN,^a
SOPHIE CRAVATTE,^a AND SYLVIE LE GENTIL^b

^a *LEGOS, Université de Toulouse, CNRS, CNES, IRD, Toulouse, France*

^b *LOPS, Université de Bretagne Occidentale, Ifremer, CNRS, IRD, Brest, France*

^c *Department of Earth System Science, Stanford University, Stanford, California*

(Manuscript received 5 August 2020, in final form 23 October 2020)

ABSTRACT: At low latitudes in the ocean, the deep currents are shaped into narrow jets flowing eastward and westward, reversing periodically with latitude between 15°S and 15°N. These jets are present from the thermocline to the bottom. The energy sources and the physical mechanisms responsible for their formation are still debated and poorly understood. This study explores the role of the destabilization of intra-annual equatorial waves in the jets' formation process, as these waves are known to be an important energy source at low latitudes. The study focuses particularly on the role of barotropic Rossby waves as a first step toward understanding the relevant physical mechanisms. It is shown from a set of idealized numerical simulations and analytical solutions that nonlinear triad interactions (NLTIs) play a crucial role in the transfer of energy toward jet-like structures (long waves with short meridional wavelengths) that induce a zonal residual mean circulation. The sensitivity of the instability emergence and the scale selection of the jet-like secondary wave to the forced primary wave are analyzed. For realistic amplitudes around 5–20 cm s⁻¹, the primary waves that produce the most realistic jet-like structures are zonally propagating intra-annual waves with periods between 60 and 130 days and wavelengths between 200 and 300 km. The NLTl mechanism is a first step toward the generation of a permanent jet-structured circulation and is discussed in the context of turbulent cascade theories.

KEYWORDS: Ocean circulation; Jets; Rossby waves; Nonlinear dynamics

1. Introduction

The deep equatorial and tropical circulation is organized into systems of alternating eastward and westward jets (Firing 1987; Firing et al. 1998; Johnson et al. 2002; Ollitrault et al. 2006; Ascani et al. 2010; Cravatte et al. 2012; Ollitrault and Colin de Verdière 2014; Qiu et al. 2013; Cravatte et al. 2017). We distinguish in particular (i) meridionally alternating off-equatorial jets with a meridional scale of $\sim 3^\circ$ within the 15°S–15°N latitude range, which have a large vertical scale (quasi barotropic), called extra-equatorial jets (EEJs) and (ii) vertically alternating equatorial jets trapped equatorward of $\sim 2^\circ$, which have a small vertical scale of ~ 350 m, called equatorial deep jets (EDJs). These jets are present from below the thermocline down to at least 2000 m, with some evidence of jets extending to the ocean bottom (Firing et al. 1998; Delpech et al. 2020a).

The underlying physical mechanisms generating these systems of jets are still poorly understood. Different physical mechanisms have been proposed to explain their formation, relying on a cascade of mechanisms transferring energy from a deep energy source (generally generated through the propagation at depth of atmospheric variability or currents instabilities) to the

mean jet-structured circulation (see Fig. 2 of Ménesguen et al. 2019).

Earlier studies have shown that two-dimensional turbulence induces an inverse cascade, with energy transferred toward larger scales. On a rotating planet, this cascade results in the emergence of zonal structures due to the anisotropy of the Coriolis parameter (i.e., the beta effect) (Rhines 1975; Vallis and Maltrud 1993). Most of these studies have, however, been conducted in a theoretical framework and have not addressed the source of the turbulence. The initiation of an inverse cascade at depth at low latitude in the oceans would indeed require the presence of strong turbulence that has not been documented yet.

One of the major energy sources present in the ocean at low latitude is associated with planetary waves. It has been shown that in the Atlantic and Pacific Oceans, a large source of energy in the deep is associated with annual and semiannual Rossby waves, as well as intra-annual waves: 30-day, 1000-km mixed Rossby–gravity waves, associated with surface tropical instability waves, and short-scale variability, with periods around 70 days and wavelengths around 500 km (Bunge et al. 2008; von Schuckmann et al. 2008; Tuchen et al. 2018; Lyman et al. 2005, 2007; Kessler and McCreary 1993; Eriksen and Richman 1988; Farrar and Weller 2006; Farrar 2011; Farrar and Durland 2012; Lee et al. 2017; Delpech et al. 2020b) (see Fig. 1 for an overview of the spectral characteristics of the observed variability).

Corresponding author: Audrey Delpech, audrey.delpech@legos.obs-mip.fr

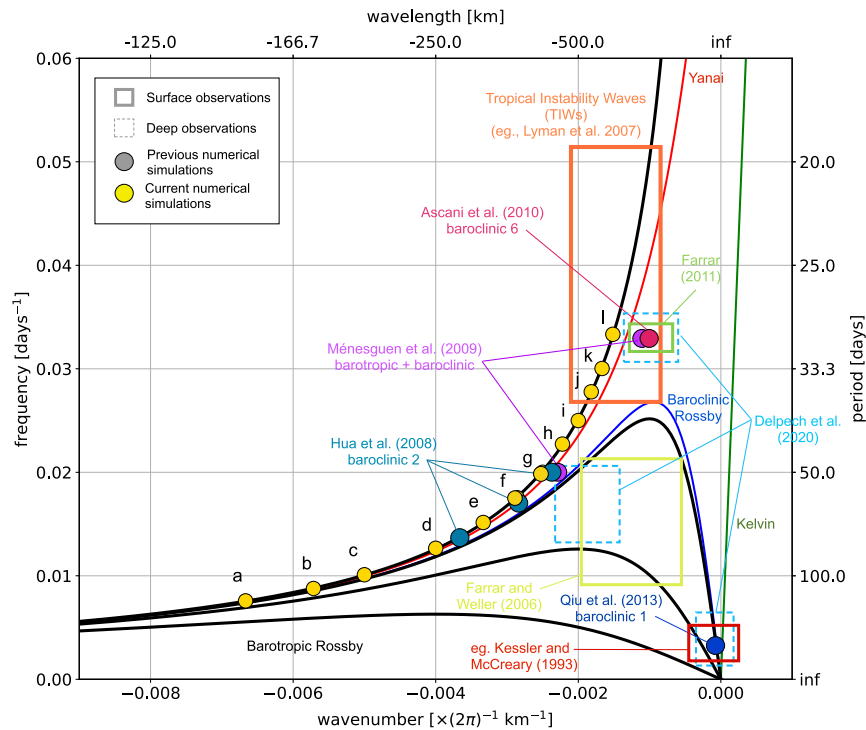


FIG. 1. Wavenumber frequency diagram with the dispersion relations for equatorial Kelvin waves (green), Yanai waves (red), and baroclinic Rossby waves (blue). Only the first baroclinic mode is represented. The dispersion relation for barotropic Rossby waves with different meridional wavenumbers (0 , 1×10^{-6} , 2×10^{-6} , and $4 \times 10^{-6} \text{ m}^{-1}$ from top to bottom) are in black. The frequency and wavenumbers of the forcing used in the experiments conducted in this study are represented by the yellow dots. Wave instability simulations conducted in previous studies are indicated with colored dots along with their references. The outlined boxes represent the spectral range of waves that have been observed at the surface (solid lines) and at depth (dashed lines).

Equatorial waves, when generated at the surface, propagate to depth. In the intra-annual range in particular, waves have steep propagation ray paths (Cox 1980) and are thus very efficient at transferring energy to the deep ocean.

These waves can develop instabilities and the destabilization of some particular planetary waves have been shown to be a potential mechanism for the formation of a jet-structured circulation (Gill 1974; Hua et al. 2008; Connaughton et al. 2010; Qiu et al. 2013; d'Orgeville et al. 2007; Ménesguen et al. 2009; Ascani et al. 2010). In an idealized model configuration forced with different intra-annual baroclinic Yanai waves (Fig. 1, gray dots), d'Orgeville et al. (2007) and Hua et al. (2008) were able to reproduce the EDJs-like structures, whose vertical scale was mainly dependent on the initial wave period. In a similar configuration forced with baroclinic Yanai waves and short barotropic Rossby waves at 50-day period (Fig. 1, magenta dots), Ménesguen et al. (2009) were able to reproduce the EDJs and the first meridionally alternating EEJs at 2°S and 2°N in equatorial dedicated experiments. Ascani et al. (2010) were able to reproduce meridionally alternating EEJs in the 5°S – 5°N latitude band, with a vertically propagating beam of a Yanai wave with a period of 30 days and a wavelength of 1000 km (Fig. 1, red dot). In an idealized reduced gravity model forced with a baroclinic mode-1 annual Rossby wave (Fig. 1, blue dot),

Qiu et al. (2013) were able to reproduce meridionally alternating EEJs in the 5° – 40°N latitude band. The configurations and characteristics of the wave forcing as well as the physical interpretation of the processes involved in these numerical experiments differ, however, from study to study. A general framework for interpreting the effects of planetary waves instability on the mean circulation is still missing. In the framework of quasigeostrophic dynamics, Gill (1974) studied the instability of barotropic Rossby waves on a beta plane, focusing on two particular asymptotic cases: the case of very weak nonlinearities (corresponding to resonant triad interactions) and the case of very strong nonlinearities. He showed that, in the limit of strong nonlinearities, Rossby waves can transfer their energy toward a zero zonal wavenumber, a nonzero meridional wavenumber, and zero frequency mode, the so-called zonal jet-like structures. Hua et al. (2008) adapted the barotropic theory of Gill (1974) to baroclinic equatorially trapped waves. They showed that equatorially trapped baroclinic waves can also be destabilized into vertically alternating and meridionally alternating jet-like structures, thus extending Gill's results to lower latitudes. Ménesguen et al. (2009) interpreted the destabilization of the barotropic Rossby waves into EEJs-like structures in their simulation using the theory of Gill (1974) in the strong nonlinear limit, while Qiu et al. (2013)

interpreted the formation of EEJs in their simulations as the destabilization of annual Rossby waves through resonant triad interactions (corresponding to the weak nonlinear limit of Gill’s theory) and to further nonlinear adjustments involving potential vorticity fluxes. In addition, all the numerical studies exploring the formation of EEJs from waves have focused on a limited set of wave periods. A general continuous framework to analyze the potential contribution of all planetary waves in generating the mean jet-structured circulation as a function of their characteristics has yet to be formulated.

In this study, our goal is to provide new insights into the mechanisms that drive the deep tropical circulation and its jet structuring, focusing on the formation of EEJs-like structures by the destabilization of planetary waves. In particular, we aim to extend previous numerical experiments to other waves, with a focus on the intra-annual waves, and to develop a general theoretical framework to compare and interpret the different experiments. This study focuses on the early stage of jet formation. We thus emphasize the mechanism of energy transfer from a primary energy source to EEJs-like structures with quasi-barotropic zonal velocities that reverse over a meridional scale of ~ 350 km and that have a long temporal coherence. We leave for further studies the long-term equilibration of these jet-like structures. We will in particular address the following questions:

- 1) What is the potential for intra-annual waves to create off-equatorial, meridionally alternating, jet-like structures?
- 2) Is there a preferential frequency and wavenumber of the waves for reproducing realistic jets?
- 3) What are the processes responsible for the transfer of energy from waves to jet-like structures?

To answer these questions, we perform idealized numerical experiments of the equatorial ocean forced by an oscillating wind stress that acts as a wavemaker and generates waves with predetermined characteristics. The idealized configuration is designed to evaluate the sensitivity of the response of each forced wave to the period and wavenumber of the forcing. As a first step, we will study the destabilization of barotropic waves using two-dimensional numerical simulations, leaving the generalization to fully three-dimensional dynamics for subsequent work. The barotropic mode offers the advantage that it is not equatorially trapped, which makes the problem invariant with latitude. It also radiates energy rapidly away from forcing regions, making it easier to simulate freely propagating waves. Evidence for purely barotropic waves in the equatorial oceans are limited to a few studies (Farrar 2011; Rohith et al. 2019; Farrar et al. 2020, manuscript submitted to *J. Phys. Oceanogr.*). The approach described in this study, however, can be generalized to baroclinic modes.

We show that the formation of jet-like structures is triggered by the nonlinear terms in the momentum equations, which allow for wave–wave interactions. A full description of the nonlinear physics is not possible, due to its intrinsic chaotic nature. We thus investigate how the waves can destabilize and produce jet-like structures within the framework of a truncated nonlinear wave interaction theory. This theory, which can be viewed as a generalization of Gill (1974), has been fully described and investigated with applications in geophysics and plasma physics (Connaughton et al. 2010) and is here adapted

to study the instability of barotropic Rossby waves. It allows for solving analytically the nonlinearity of the system, assuming a limited number of wave interactions, with a continuity from a weakly nonlinear regime to a strongly nonlinear regime, for any primary wave spectral characteristics.

The remainder of this paper is organized as follows. The numerical model configuration, forcing, and wave field used in the experiments are described in section 2. The spectral method using wavelets transform that is used to analyze the waves in the simulations is described in section 3. The results of the numerical experiments are described in section 4. The instability that develops in the nonlinear simulations is compared to the prediction from the three-mode truncation nonlinear triad interaction (NLTI) analytical model in section 5. The sensitivity of the creation of jet-like structures to the wavenumber and frequency of the forced wave is investigated in section 6. We end the article with a discussion of how the results support and complement previous studies, and we summarize the main results and provide perspectives for future work.

2. Numerical experiments

a. Model description

The idealized simulations performed in this study are run with the Coastal and Regional Community (CROCO) model. The CROCO model solves the primitive equations (Shchepetkin and McWilliams 2005, 2009) with a time-splitting method between the fast barotropic mode and the slow baroclinic modes. The model is used in its barotropic configuration, which solves the vertically integrated momentum equations (Shchepetkin and O’Brien 1996; Shchepetkin and McWilliams 2009):

$$(hu)_t + (hu^2)_x + (huv)_y - fhw + gh\eta_x = \mathcal{F}^u + \mathcal{D}^u, \quad (1a)$$

$$(hv)_t + (huv)_x + (hv^2)_y + fhu + gh\eta_y = \mathcal{F}^v + \mathcal{D}^v, \quad \text{and} \quad (1b)$$

$$h_t + (hu)_x + (hv)_y = 0 \quad (1c)$$

where (u, v) is the barotropic velocity vector, $h(x, y, t) = H + \eta(x, y, t)$ is the total water depth, η is the free surface elevation, H is the water depth at rest, g is the gravity constant, and f is the Coriolis parameter. Parameters \mathcal{F} and \mathcal{D} represent forcing and frictional terms, respectively.

b. Model configuration

The basin configuration is meant to represent an idealized ocean at low latitudes. Its size is $140^\circ \times 70^\circ \times 5000$ m (longitude \times latitude \times depth), and it is centered on the equator. The horizontal resolution is $0.25^\circ \times 0.25^\circ$. The Coriolis parameter follows the variations of an equatorial beta plane, $f = \beta y$, where $\beta = 2.3 \times 10^{-11} \text{ (m s)}^{-1}$ is the planetary vorticity gradient and y is the meridional position from the equator.

The model is forced with a surface stress $\tau = (\tau^x, \tau^y)$, which is incorporated in the model equations [Eq. (1)] as a surface momentum forcing (SMF) $\mathcal{F}^u = \tau^x/\rho_0$ and $\mathcal{F}^v = \tau^y/\rho_0$. Because our objective is to generate freely propagating intra-annual waves, the surface stress is localized inside a specific region and takes the form of a wavemaker [Eq. (2)]:

TABLE 1. Summary of all numerical experiments used for this study, where T_0 , ω_0 , λ_{x0} , k_{x0} , and τ_0/ρ_0 are the period, frequency, zonal wavelength, zonal wavenumber, and amplitude of the forcing [Eq. (2)]. The experiments are 2D and are either linear (L) or nonlinear (NL). The letter of the experiment label indicates its position on the wavenumber–frequency spectrum (Fig. 1), and the number indicates the forcing amplitude.

Expt	T_0 (days)	ω_0 (s ⁻¹)	λ_{x0} (km)	k_{x0} (m ⁻¹)	τ_0/ρ_0 (m ² s ⁻²)	Physics	
1a	132	5.49×10^{-7}	150	4.19×10^{-5}	5×10^{-5}	2D	NL
1b	114	6.41×10^{-7}	175	3.59×10^{-5}	5×10^{-5}	2D	NL
1c	99	7.32×10^{-7}	200	3.14×10^{-5}	5×10^{-5}	2D	NL
1d	79	9.15×10^{-7}	250	2.51×10^{-5}	5×10^{-5}	2D	NL
1e	66	1.10×10^{-6}	300	2.09×10^{-5}	5×10^{-5}	2D	NL
1f	57	1.28×10^{-6}	350	1.80×10^{-5}	5×10^{-5}	2D	NL
1g	50	1.46×10^{-6}	400	1.57×10^{-5}	5×10^{-5}	2D	NL
1h	44	1.65×10^{-6}	450	1.40×10^{-6}	5×10^{-5}	2D	NL
1i	40	1.83×10^{-6}	500	1.26×10^{-5}	5×10^{-5}	2D	NL
1j	36	2.01×10^{-6}	550	1.14×10^{-5}	5×10^{-5}	2D	NL
1k	33	2.2×10^{-6}	600	1.0×10^{-5}	5×10^{-5}	2D	NL
1l	30	2.4×10^{-6}	650	9.7×10^{-6}	5×10^{-5}	2D	NL
2a	132	5.49×10^{-7}	150	4.19×10^{-5}	5×10^{-6}	2D	NL
2c	99	7.32×10^{-7}	200	3.14×10^{-5}	5×10^{-6}	2D	NL
2e	66	1.10×10^{-6}	300	2.09×10^{-5}	5×10^{-6}	2D	NL
2g	50	1.46×10^{-6}	400	1.57×10^{-5}	5×10^{-6}	2D	NL
2i	40	1.83×10^{-6}	500	1.26×10^{-5}	5×10^{-6}	2D	NL
3a	132	5.49×10^{-7}	150	4.19×10^{-5}	2.5×10^{-5}	2D	NL
3c	99	7.32×10^{-7}	200	3.14×10^{-5}	2.5×10^{-5}	2D	NL
3e	66	1.10×10^{-6}	300	2.09×10^{-5}	2.5×10^{-5}	2D	NL
3g	50	1.46×10^{-6}	400	1.57×10^{-5}	2.5×10^{-5}	2D	NL
3i	40	1.83×10^{-6}	500	1.26×10^{-5}	2.5×10^{-5}	2D	NL
4a	132	5.49×10^{-7}	150	4.19×10^{-5}	7.5×10^{-5}	2D	NL
4c	99	7.32×10^{-7}	200	3.14×10^{-5}	7.5×10^{-5}	2D	NL
4e	66	1.10×10^{-6}	300	2.09×10^{-5}	7.5×10^{-5}	2D	NL
4g	50	1.46×10^{-6}	400	1.57×10^{-5}	7.5×10^{-5}	2D	NL
4i	40	1.83×10^{-6}	500	1.26×10^{-5}	7.5×10^{-5}	2D	NL
5a	132	5.49×10^{-7}	150	4.19×10^{-5}	1×10^{-4}	2D	NL
5c	99	7.32×10^{-7}	200	3.14×10^{-5}	1×10^{-4}	2D	NL
5e	66	1.10×10^{-6}	300	2.09×10^{-5}	1×10^{-4}	2D	NL
5g	50	1.46×10^{-6}	400	1.57×10^{-5}	1×10^{-4}	2D	NL
5i	40	1.83×10^{-6}	500	1.26×10^{-5}	1×10^{-4}	2D	NL
6a	132	5.49×10^{-7}	150	4.19×10^{-5}	1.5×10^{-4}	2D	NL
6c	99	7.32×10^{-7}	200	3.14×10^{-5}	1.5×10^{-4}	2D	NL
6e	66	1.10×10^{-6}	300	2.09×10^{-5}	1.5×10^{-4}	2D	NL
6g	50	1.46×10^{-6}	400	1.57×10^{-5}	1.5×10^{-4}	2D	NL
6i	40	1.83×10^{-6}	500	1.26×10^{-5}	1.5×10^{-4}	2D	NL
1d-L	79	9.15×10^{-7}	250	2.51×10^{-5}	5×10^{-5}	2D	L
1l-L	30	2.4×10^{-6}	650	9.7×10^{-6}	5×10^{-5}	2D	L

$$\tau^x = -\tau_0 X(x)Y(y) \sin(\mathbf{k}_0 \cdot \mathbf{x} - \omega_0 t) (k_{y0}/k_{x0}) \quad \text{and} \quad (2a)$$

$$\tau^y = \tau_0 X(x)Y(y) \sin(\mathbf{k}_0 \cdot \mathbf{x} - \omega_0 t), \quad (2b)$$

where $X(x)$ and $Y(y)$ are envelope profiles. With this choice of wavemaker, τ will generate a plane wave of streamfunction $\psi = \psi_0 \cos(\mathbf{k}_0 \cdot \mathbf{x} - \omega_0 t)$. Unless specified differently, we take $k_{y0} = 0$ for all experiments, which leads to $\tau^x = 0$. The generated waves thus have a strong meridional component of the velocity and propagate zonally, as are the characteristics of the observed intra-annual waves. The SMF wavenumber k_{x0} , frequency ω_0 , and amplitude τ_0 differ for each experiment (Table 1). The containment of the wavemaker inside a localized forcing region $X(x)Y(y)$ is essential to have an unforced region where the different waves can freely propagate

without interference by the forcing. It is also more realistic as most intra-annual waves observed in the ocean are found to be locally generated and vary spatially (e.g., Tuchen et al. 2018; Delpech et al. 2020b). The envelope of this forcing region is defined following Eq. (3) below; it is similar to a Blackman window of size (x_w, y_w) centered on (x_0, y_0) :

$$X(x) = \tanh\left(\frac{x - x_0 - 0.5x_w}{x_t}\right) - \tanh\left(\frac{x - x_0 + 0.5x_w}{x_t}\right) \quad \text{and} \quad (3a)$$

$$Y(y) = \tanh\left(\frac{y - y_0 - 0.5y_w}{y_t}\right) - \tanh\left(\frac{y - y_0 + 0.5y_w}{y_t}\right) \quad (3b)$$

where (x_0, y_0) is the position of the center of the forcing region, x_w and y_w are the widths of the forcing region, and x_t and y_t are the tapering extent of the forcing region. Unless specified differently, the forcing region is centered in the middle of the basin $(x_0, y_0) = (70^\circ, 0^\circ)$. The other parameters are taken by default as $x_w = 20^\circ$, $y_w = 15^\circ$, $x_t = 5^\circ$, and $y_t = 2^\circ$. Note that the exact location of the forcing region does not influence the outcome of the simulations. As the barotropic Rossby deformation radius is very large, the propagation of barotropic Rossby waves does not depend on latitude and are not subject to beta dispersion (Schopf et al. 1981). Test simulations have been conducted with $y_0 = 15^\circ$, without substantial modifications to the results (not shown). Similarly, the conclusions of this study are not sensitive to the extension of the forcing region. Test experiments have been conducted with $y_w = 5^\circ$ and $y_w = 25^\circ$ (not shown). The size of the forcing region controls the energy input into the ocean and changes the amplitude of the wave response. This sensitivity is thus similar to the sensitivity to the SMF amplitude (τ_0), which is fully investigated in section 6. The characterization of the oceanic response to the forcing is investigated in section 2c and examples are given in section 4 and illustrate that for the range of parameters considered, the envelope does not affect the wave response.

All lateral boundaries are closed with free slip boundary conditions. A sponge layer is implemented on the northern and southern boundaries to avoid the propagation of artificial coastal waves. In the sponge layers, the lateral viscosity is increased toward the northern and southern boundaries. The bottom is flat and a linear bottom drag law is applied to balance the energy input from the forcing. Therefore, the frictional terms in the equations are

$$D_u = -\alpha u + D_0 \{ \tanh[(y - y_s)/dy_s] + \tanh[(y + y_s)/dy_s] \} / 2 \quad \text{and}$$

$$D_v = -\alpha v + D_0 \{ \tanh[(y - y_s)/dy_s] - \tanh[(y + y_s)/dy_s] \} / 2,$$

with $\alpha = 1.5 \times 10^{-4} \text{ m s}^{-1}$, $D_0 = 5000 \text{ m}^2 \text{ s}^{-1}$, $y_s = 34^\circ$, and $dy_s = 1^\circ$. No explicit horizontal viscosity is included in the basin interior. The horizontal momentum equations are discretized using a third-order upstream scheme, which has implicit diffusion.

The initial condition is a state at rest with zero velocity and no free surface elevation. The model is used in nonlinear and linear configurations. In the case of linear simulations, the nonlinear advection terms $\mathbf{u} \cdot \nabla \mathbf{u}$ are discarded from Eq. (1).

c. Wave generation

To study the instability of barotropic Rossby waves and their role in the formation of jet-like structures, we aim to create freely propagating waves using the surface momentum flux described in Eq. (2). Because the direct response to the SMF is not in geostrophic equilibrium, an adjustment occurs by radiating many different types of waves. The objective is to ensure that the wave with the characteristics of the forcing (i.e., with wavevector \mathbf{k}_0 and frequency ω_0) is the wave that contains most of the energy, which we will call hereinafter the primary wave. If the wavevector that contains most energy and the forcing frequency ω_0 satisfy the dispersion relation for barotropic Rossby waves

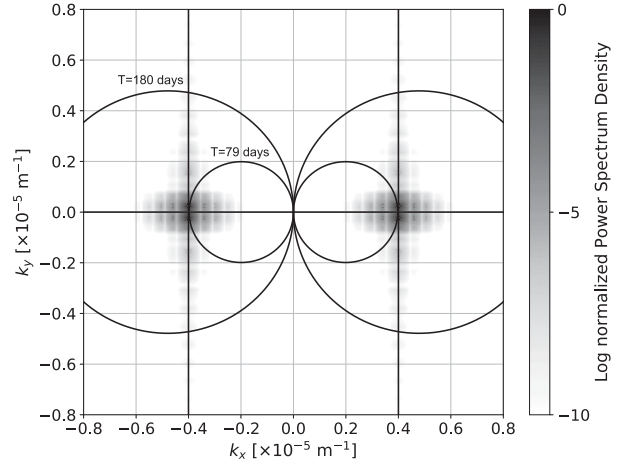


FIG. 2. Two-dimensional spectrum of the wind stress function $F(x, y, t) = X(x)Y(y) \sin(k_{x0}x + k_{y0}y - \omega_0 t)$ (gray) for simulation 1d (see Table 1). Black straight lines correspond to the forced wave number $\pm k_{x0}$ and $k_{y0} = 0$. Black circles correspond to the barotropic Rossby wave dispersion relation for the forced frequency ω_0 ($T = 79$ days) and a nonresonant frequency ($T = 180$ days). If the dispersion relation intersects a location in wavenumbers space where there is a maximum in energy, the forced wave is resonantly forced. The example shows that only the period corresponding to the barotropic Rossby wave dispersion relation for k_{x0} and k_{y0} satisfies the resonant condition.

$$\omega = \frac{-\beta k_x}{k_x^2 + k_y^2 + F} \quad (4)$$

then this wave will be resonantly forced, where (k_x, k_y) is the wavevector, ω the wave frequency, and F the inverse of the Rossby deformation radius squared. In this study, we focus on the barotropic mode, $F = (1/R_{d0}^2)$, with R_{d0} being the barotropic Rossby deformation radius. In the equatorial regions, R_{d0} is very large (i.e., $R_{d0} \sim 4500 \text{ km}$ at 20° , the poleward limit of the domain that we are using), and thus the upper limit of F in this region is $\sim 10^{-14} \text{ m}^{-2}$, which is smaller than the wavenumbers considered (typically $|\mathbf{k}|^2 \sim 10^{-10} \text{ m}^{-2}$). In the following, we thus consider $F \sim 0$.

Because the SMF wavemaker is modulated by the envelope, its spatial spectral footprint is spread over a range of wave number (Fig. 2). Its energy maximum in wavenumber space is, however, found close to \mathbf{k}_0 , and intersects the Rossby wave dispersion relation for the frequency ω_0 , thus satisfying the resonant condition. It is ensured that all the experiments conducted in this study (Table 1) satisfy this condition.

In the case of resonant SMF, the primary wave in the simulations is a barotropic wave with the characteristics of the forcing function (i.e., wavevector \mathbf{k}_0 and frequency ω_0) that propagates along the ray paths defined by the integration of the group velocity vector (C_{gx}, C_{gy}) :

$$C_{gx} = \frac{\beta(k_x^2 - k_y^2)}{(k_x^2 + k_y^2)^2} \quad \text{and} \quad (5a)$$

$$C_{gy} = \frac{2\beta k_x k_y}{(k_x^2 + k_y^2)^2}. \quad (5b)$$

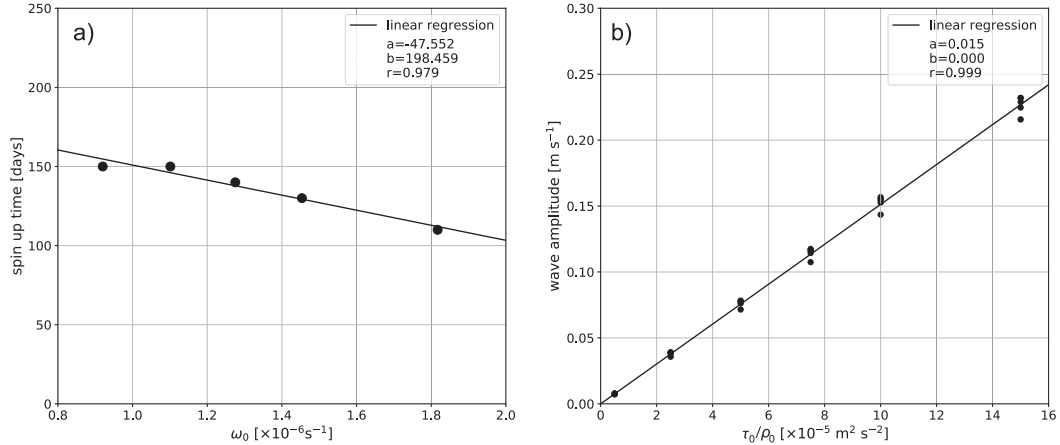


FIG. 3. (a) Experiment spinup time [computed as in Eq. (6)] as a function of the forcing frequency ω_0 . (b) Amplitude of the wave response [computed as in Eq. (7)] as a function of the strength of the forcing τ_0/ρ_0 for experiments a–l (Fig. 1). The best linear fit (line) corresponds to a line $y = ax + b$, and r is the correlation coefficient.

Because the initial state of the simulations is at rest, there is a spinup time that corresponds to the time it takes for the forcing to transfer energy to the oceanic response and balance the different dissipation terms. The spinup time and the amplitude of the response can vary for the different experiments. It is important to evaluate both quantities to get the best possible description of the generated primary wave, since the characteristics of the primary wave determine the properties of the secondary waves (sections 5 and 6).

We define the spinup time for a wave forced at \mathbf{k}_0 and ω_0 [Eq. (2)] as $S_{\mathbf{k}_0, \omega_0}$, the time at which the energy reaches 60% of its maximal value:

$$S_{\mathbf{k}_0, \omega_0} = \min_{t \in \chi} [\overline{\text{KE}}(t) - 0.6 \times \overline{\text{KE}}_{\max} > 0], \quad (6)$$

where $\overline{\text{KE}}$ is the spatial average of the kinetic energy over the spatial domain of the simulation (Ω), χ is the total duration of the simulation. The spinup time decreases slightly toward higher forcing frequencies, but the values remain around 100–150 days (Fig. 3a).

We define the amplitude for a wave forced at \mathbf{k}_0 and ω_0 [Eq. (2)] as $A_{\mathbf{k}_0, \omega_0}$, the average of the highest velocities' values in the forcing region:

$$A_{\mathbf{k}_0, \omega_0} = \frac{1}{\Omega S_{\mathbf{k}_0, \omega_0}} \int_0^{S_{\mathbf{k}_0, \omega_0}} \iint_{\Omega} v_{\mathbf{k}_0, \omega_0}(x, y, t) H[v_{\mathbf{k}_0, \omega_0}(x, y, t) - v_{\mathbf{k}_0, \omega_0}^*] dx dy dt, \quad (7)$$

where $v_{\mathbf{k}_0, \omega_0}$ is the meridional velocity in a simulation forced by \mathbf{k}_0 and ω_0 [Eq. (2)], $v_{\mathbf{k}_0, \omega_0}^*$ is the 95th percentile of the distribution of v in the forcing region $X(x)Y(y)$ [Eq. (3)], H is the Heaviside function, and Ω is the simulation domain. The amplitude of the forced wave varies linearly with the magnitude of the SMF (Fig. 3b).

d. Experimental design

Table 1 summarizes all the experiments used and described in this study. The simulations are chosen to span the intra-annual period range from 30 to 130 days with primary waves that follow the dispersion relation for barotropic Rossby waves

with zero meridional wavenumber (experiments a–l in Fig. 1). These $k_y = 0$ primary waves are found to be the optimal waves to produce jet-like structures, as will be shown in section 6b. For this reason, our simulations focus on this particular wave type. All experiments (a–l) are run for a nominal SMF amplitude of $\tau_0/\rho_0 = 5 \times 10^{-5} \text{ m}^2 \text{ s}^{-2}$ (simulation 1). Experiments a, c, e, g, and i are run with for $\tau_0/\rho_0 = 5 \times 10^{-6} \text{ m}^2 \text{ s}^{-2}$ (simulation 2), $\tau_0/\rho_0 = 2.5 \times 10^{-5} \text{ m}^2 \text{ s}^{-2}$ (simulation 3), $\tau_0/\rho_0 = 7.5 \times 10^{-5} \text{ m}^2 \text{ s}^{-2}$ (simulation 4), $\tau_0/\rho_0 = 1.0 \times 10^{-4} \text{ m}^2 \text{ s}^{-2}$ (simulation 5), and $\tau_0/\rho_0 = 1.5 \times 10^{-4} \text{ m}^2 \text{ s}^{-2}$ (simulation 6). All simulations are run with a nonlinear physics (NL), and simulations 1a and 1l are repeated using a linear physics (L). The simulations are run for 1800 days (5 years), with output every 10 days.

3. Spectral analysis method

One objective of the analysis of the simulations is to quantify the primary wave destabilization and transfer of energy between wave modes by NLTI. Spectral analyses are the ideal tool for this task. Because the properties of the waves and their spectral content are expected to change in space and time, we compute local spectra using wavelet transforms (Graps 1995; Gargour et al. 2009).

a. Wavelet transform

A continuous wavelet transform using a complex Morlet wavelet (Lee et al. 2019) is applied to the velocity field (u, v). This method results in an estimation of the amplitude of the velocity signal contained in each frequency $[\tilde{v}^x(\omega; x, y, t)]$ and wavenumber $[\tilde{v}^x(k_x; x, y, t), \tilde{v}^y(k_y; x, y, t)]$ at each location $(x, y) \in \Omega$ of the domain Ω and each time $t \in \chi$ of the simulation, over the time interval χ .

We define the spatially averaged one-dimensional spectral kinetic energy as

$$\overline{\text{KE}}^x(\hat{x}; x, y, t) = \frac{1}{\Omega} \iint_{\Omega} [|\tilde{u}^x(\hat{x}; x, y, t)|^2 + |\tilde{v}^x(\hat{x}; x, y, t)|^2] dx dy, \quad (8)$$

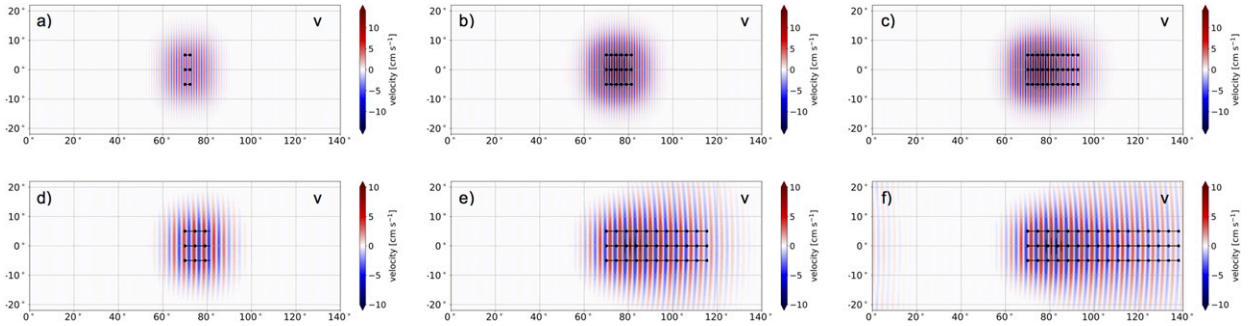


FIG. 4. Evolution of the meridional barotropic velocity v in the linear simulations (a)–(c) 1d-L and (d)–(f) 1l-L at times (left) $t = 100$ days, (center) $t = 400$ days, and (right) $t = 800$ days. Black lines indicate the ray path originating from 70° longitude (the center of the forcing region) and -5° , 0° , and 5° latitude, respectively, and integrated from the initial time of the simulation to the time of the snapshot [Eq. (5)]. The position of the ray at each wave period is indicated by the dots. The zonal barotropic velocity u is almost zero in the whole basin and is not shown.

where $x_i \in \{x, y, t\}$ and \hat{x}_i is the spectral variable along the x_i dimension (including frequency). Note that this definition of the one-dimensional spectral kinetic energy differs from the wavelet transform of the kinetic energy $[(u^2 + v^2)/2]$ and has the advantage of retaining the spectral scales of the velocity field. The spectral dimensions and their resolution are chosen as follows: we estimate the temporal wavelet transform for periods from 10 to 350 days with a 3.3-day interval and the spatial wavelet transform for wavelengths from 90 to 3700 km with an 18.5-km interval. The wavelet transform amplitude cannot be accurately estimated for locations close to the boundaries of the simulation domain and for times close to the beginning and the end of the simulations (especially for long wavelengths and periods). This is known as the cone of influence (Torrence and Compo 1998). Estimates that lie within the cone of influence are thus discarded.

b. Two-dimensional spectra from wavelet transform

A wavelet analysis provides a one-dimensional spectrum as the spectral transform is computed on each physical dimension separately. To correlate this information, we construct cross-product spectra $\hat{q}^{x_i x_j}$ of a quantity q along the spectral dimension \hat{x}_i, \hat{x}_j as defined by Eq. (9):

$$\hat{q}^{x_i x_j}(\hat{x}_i, \hat{x}_j; t) = \frac{1}{\Omega} \iint_{\Omega} |\tilde{q}^{x_i}(\hat{x}_i; x, y, t)|^2 |\tilde{q}^{x_j}(\hat{x}_j; x, y, t)|^2 dx dy, \quad (9)$$

where $x_i, x_j \in \{x, y, t\}$ and \hat{x}_i is the spectral variable along the x_i dimension. Note that $\hat{q}^{x_i x_j}$ is equivalent to the two-dimensional Fourier transform but also varies in time.

We define the two-dimensional spectral kinetic energy as

$$\widehat{\text{KE}}^{x_i x_j}(\hat{x}_i, \hat{x}_j; t) = \widehat{u}^{x_i x_j}(\hat{x}_i, \hat{x}_j; t) + \widehat{v}^{x_i x_j}(\hat{x}_i, \hat{x}_j; t). \quad (10)$$

4. Numerical solutions

a. Propagation of the forced waves in the linear simulations

The linear simulations illustrate the key features of each experiment and help to ensure that the dominant signal generated by the SMF is associated with the forced primary wave

(section 2c). In simulations 1d and 1l (Fig. 4), waves with a strong signature in meridional velocity propagate eastward of the forcing region. These waves have the characteristics (i.e., wavenumber and frequency) of the forcing (not shown). Their energy propagation follows the theoretical ray paths predicted from the dispersion relation. The propagation is much faster for high-frequency, long-wavelength forcing (Figs. 4d–f) than for low-frequency, short-wavelength forcing (Figs. 4a–c). Note that there is also a slight spreading of the energy in the meridional direction when the wave propagates eastward. Barotropic waves are plane waves and are thus invariant in the direction perpendicular to their propagation direction (the meridional direction in the case of the two examples). The relaxation of the forced solution [which is not an exact plane wave due to the nonzero k_y , associated with the envelope $X(x)Y(y)$] toward a free plane wave solution outside of the forcing region can thus explain the meridional spread of the wave signature. These linear simulations confirm that the SMF excites principally a barotropic Rossby wave with the forcing characteristics, as expected from the chosen idealized setup (section 2b).

b. Propagation of the forced wave and secondary waves in nonlinear simulations

When the nonlinear terms are taken into account in the model [Eq. (1)], the key features of some simulations is modified. For example, in simulation 1d, in addition to the eastward propagation of energy associated with the forced primary wave (section 4a), there is also westward energy propagation (Figs. 5a–i). This westward propagation is associated with a wave with quasi-zonal phase lines and has a dominant signature in the zonal velocity and sea surface height. This suggests that an additional wave (aside from the forced wave) is also present in the simulation. Conversely, for other simulations forced by different wavenumbers and frequencies, such as simulation 1l, the nonlinear response does not differ much from the linear response (Figs. 5j–r and 4d–f).

c. Resulting jet-like mean flows in the nonlinear simulations

The secondary wave that develops in simulation 1d generates zonal velocities that are coherent over a large zonal extension (i.e., from 0° to 60°) and that change signs over short meridional

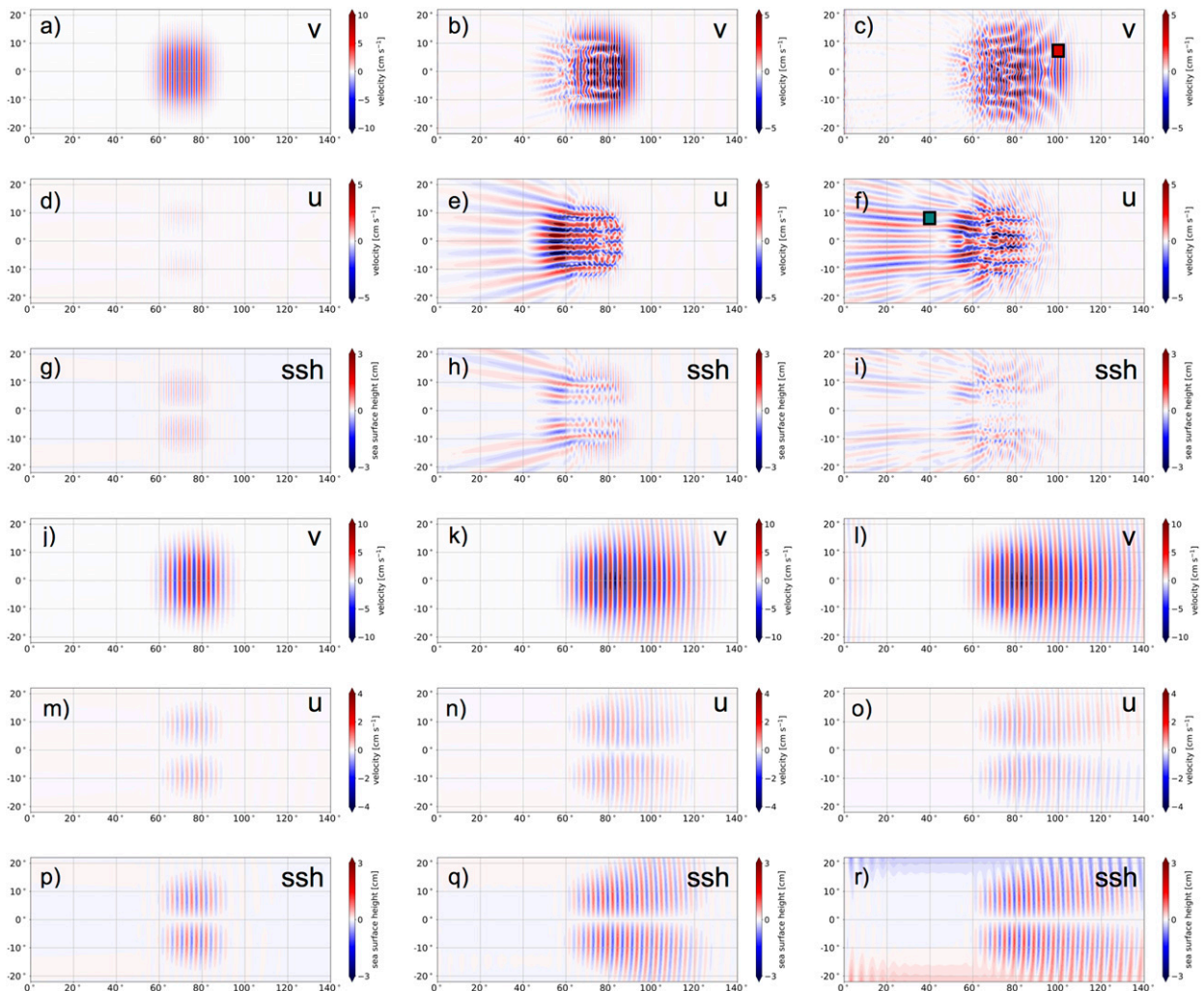


FIG. 5. Evolution of the velocity and sea surface height (ssh) in the nonlinear simulations (a)–(i) 1d and (j)–(r) 1l at times (left) $t = 100$ days; (center) $t = 400$ days; and (right) $t = 800$ days for (a)–(c), (j)–(l) v (meridional velocity); (d)–(f), (m)–(o) u (zonal velocity); and (g)–(i), (p)–(r) sea surface height. The red and green squares correspond to the locations where the one-dimensional spectra are computed (Fig. 9).

scales (i.e., every 2.5°) (Fig. 5f). When temporally averaged, this wave results in a jet-like mean flow (Fig. 6). By jet-like mean flow, we specify a circulation that shares common characteristics with the observed jet-structured circulation in the equatorial and tropical oceans (e.g., Ollitrault et al. 2006; Cravatte et al. 2012; Maximenko et al. 2005), that has meridionally alternating zonal velocities with amplitudes around $0.03\text{--}0.05\text{ m s}^{-1}$, that has sea surface height anomalies of around $2\text{--}3\text{ cm}$ that alternate sign on short meridional scales (typically $1^\circ\text{--}2^\circ$), and that has zonal and temporal coherence over thousand kilometers and several years, respectively (see also section 1).

The average over the last three years of the simulations shows that simulation 1d develops jet-like mean flow (Fig. 6a), even if its characteristics are not fully realistic (Fig. 6c); namely, the meridional scale (2°) is slightly larger than what is observed in the Pacific Ocean (1.5°) and the amplitude (0.01 m s^{-1}) is weaker than in the observations (0.06 m s^{-1}).

In contrast, simulation 1l does not develop a jet-like mean flow (Fig. 6b). The generation of jet-like mean flows and their characteristics (meridional scale, amplitude) thus strongly depend on the characteristics of the forced waves.

The aim of the remainder of this paper is to understand the origin of the secondary wave that generates jet-like mean flows, and to understand in what conditions they develop and what their characteristics are. We investigate the physical mechanisms in simulation 1d in depth before examining the sensitivity of this mechanism to the primary wave characteristics using multiple experiments (section 2d).

5. Evidence for nonlinear triadic instability in the numerical simulations

In this section, we focus on one particular experiment, simulation 1d (Table 1), to describe the secondary wave and

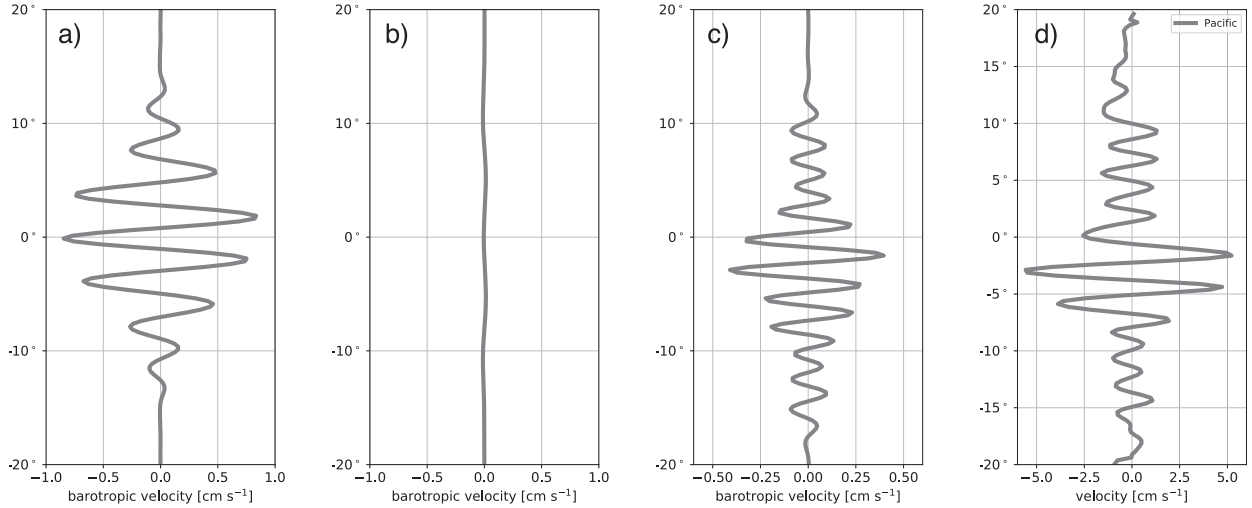


FIG. 6. Barotropic velocity u averaged over years 2–5 of the simulations from 10° to 40° of longitude (i.e., west of the forcing region) for simulations (a) 1d and (b) 1l and (c) a simulation with optimal primary wave characteristics, corresponding to experiment 1c from Table 1 but with a shifted wind stress position ($y_0 = 3^\circ\text{S}$). Also shown is (d) observed zonal velocity at 1000-m depth in the tropical Pacific from the Argo floats YoMaHA database (Lebedev et al. 2007), reproduced after Delpech et al. (2020b).

explain it in the framework of a three-mode truncation NLTI model. An analytical solution can be derived for the evolution of the primary wave streamfunction, by limiting its nonlinear interactions to a single triad, with three waves exchanging energy. The growth rate σ of this instability, which determines the two secondary waves with wavevectors \mathbf{q} and $\mathbf{p} - \mathbf{q}$ that interact with the primary wave with wavevector \mathbf{p} in a triad ($\mathbf{p} = \mathbf{q} + \mathbf{p} - \mathbf{q}$), is given by Eq. (11) and is derived analytically in the appendix, following Connaughton et al. (2010):

$$\sigma = \text{Im} \left\{ \frac{1}{2} \left[\Delta \pm \sqrt{\Delta^2 - 4|\psi_{\mathbf{p}}|^2 T(\mathbf{q}, \mathbf{p}, \mathbf{q} - \mathbf{p}) T(\mathbf{p} - \mathbf{q}, \mathbf{p}, -\mathbf{q})} \right] \right\}, \quad (11)$$

where $\Delta = \omega_{\mathbf{p}} - \omega_{\mathbf{q}} - \omega_{\mathbf{p}-\mathbf{q}}$ is the resonant triad condition (the triad is resonant if $\Delta = 0$), $T(\mathbf{k}, \mathbf{k}_i, \mathbf{k}_j) = -[(\mathbf{k}_i \times \mathbf{k}_j)_z (k_i^2 - k_j^2)]/k^2$, and Im designates the imaginary part. The growth rate depends on the wavevector (\mathbf{p}), frequency ($\omega_{\mathbf{p}}$), and amplitude of the streamfunction ($|\psi_{\mathbf{p}}|$) of the primary wave. Note that the triad instability described by this model is more general than the resonant triad instability (e.g., Pedlosky 2013). The approach is very similar to that of Gill (1974). Whereas Gill (1974) explored the weakly nonlinear limit $|\psi_{\mathbf{p}}|p^3/\beta \ll 1$ (leading to triad resonance) and the strongly nonlinear limit $|\psi_{\mathbf{p}}|p^3/\beta \gg 1$ as two separate instabilities, the analytical solution used here is a continuous function of the primary wave amplitude $|\psi_{\mathbf{p}}|$. Given the characteristics of the primary wave, Eq. (11) allows one to

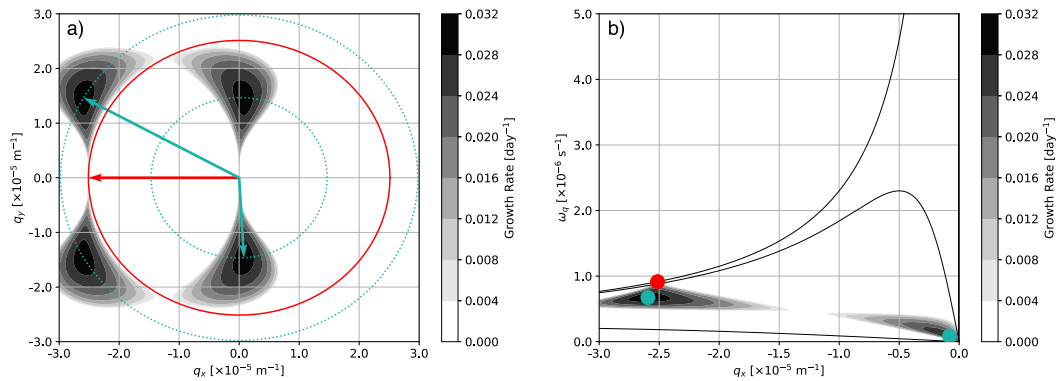


FIG. 7. (a) The growth rate for the three-mode truncated nonlinear triad interaction [Eq. (11)] as a function of the secondary wavenumbers q_x and q_y . The red arrow indicates the primary wave \mathbf{p} , and the green arrows are the most unstable secondary waves \mathbf{q} and $\mathbf{p} - \mathbf{q}$. The circles represent the magnitude of the wavevectors. (b) The growth rate as a function of the secondary wavenumber q_x and period $\omega_{\mathbf{q}}$. The red dot indicates the position of the primary wave, and the green dots are the position of the secondary waves in $\omega_{\mathbf{q}} - q_x$ space. Black lines indicate the dispersion relations for barotropic Rossby waves with $k_y = 0$ and $k_y = 2 \times 10^{-6} \text{ m}^{-1}$. The two secondary waves have the same growth rate. Note that we use the convention of positive frequency for waves, such that the wavevector with $q_x > 0$ (and thus a theoretical negative frequency) in (a) is represented with $q_x < 0$ and a positive frequency in (b).

TABLE 2. The waves involved in nonlinear triad interactions. The primary wave is the forced wave; $\omega_{\mathbf{p}}$, p_x , and p_y thus are fixed by the forcing. As the experiment is resonantly forced for the barotropic mode, they satisfy the barotropic Rossby wave dispersion relation. The properties of the two secondary waves (\mathbf{q} and $\mathbf{p}^- = \mathbf{p} - \mathbf{q}$) are determined from where the growth rate is maximum in spectral space [Eq. (11)].

	Forced wave (primary wave)	Long secondary wave	Short secondary wave
k_x (m^{-1})	$p_x = -2.3 \times 10^{-5}$	$q_x = -2.1 \times 10^{-6}$	$p_x^- = -2.0 \times 10^{-5}$
λ_x (km)	$\lambda_{\mathbf{p}x} = 250$ km	$\lambda_{\mathbf{q}x} = 4958$ km	$\lambda_{\mathbf{p}^-x} = 238$ km
k_y (m^{-1})	$p_y = 0$	$q_y = 1.4 \times 10^{-5}$	$p_y^- = 1.7 \times 10^{-5}$
λ_y (km)	$\lambda_{\mathbf{p}y} \sim \infty$	$\lambda_{\mathbf{q}y} = 429$ km	$\lambda_{\mathbf{p}^-y} = 429$ km
ω (s^{-1})	$\omega_{\mathbf{p}} = 9.8 \times 10^{-7}$	$\omega_{\mathbf{q}} = 2.6 \times 10^{-7}$	$\omega_{\mathbf{p}^-} = 7.2 \times 10^{-7}$
T (days)	$T_{\mathbf{p}} = 79$ days	$T_{\mathbf{q}} = 540$ days	$T_{\mathbf{p}^-} = 110$ days

determine the secondary waves wavevectors, \mathbf{q} and $\mathbf{p} - \mathbf{q}$, that yield the maximum growth rate. These waves are the ones most likely to emerge from nonlinear interactions.

a. Theoretical prediction for instability growth rate and secondary waves

We compute the growth rate given by Eq. (11) for the primary wave \mathbf{p} of simulation 1d (Fig. 7). The secondary waves \mathbf{q} and $\mathbf{p} - \mathbf{q}$ that will develop as predicted by theory are determined by the maxima of this growth rate. The growth rate maximum is found numerically using a wavevector grid spanning from -5×10^{-5} to $5 \times 10^{-5} \text{ m}^{-1}$ in both the k_x and k_y directions with a resolution of 10^{-7} m^{-1} . The two secondary waves resulting in the fastest growth have different characteristics. The first one has a long zonal wavelength (~ 5000 km), a short meridional wavelength (~ 430 km) (Fig. 7a), and a long period (~ 1.5 years) (Fig. 7b), called hereinafter the long secondary wave. The second one has a short zonal wavelength (~ 340 km, similar to the one of the primary wave), a short meridional wavelength (~ 430 km) (Fig. 7a), and a short period (~ 4 months) (Fig. 7b), called hereinafter the short secondary wave. The exact wavenumbers and frequencies associated with each of these waves are listed in Table 2. The long secondary wave thus has characteristics similar to the jet-like structures.

The growth rate of the secondary waves is $\sigma_{\max} = 0.032 \text{ day}^{-1}$ (Fig. 7). The primary wave is very unstable to NLTI because σ_{\max}^{-1} is of the same order of magnitude as its period. We define the time of emergence of the instability as

$$T_{\mathbf{p}}^c = \frac{5}{\sigma_{\max}}; \text{ such that } \psi_{\mathbf{q}}(T_{\mathbf{p}}^c) = e^5 \psi_{\mathbf{q}}(0) \simeq 10^2 \psi_{\mathbf{q}}(0), \quad (12)$$

where σ_{\max} is the maximum growth rate of the instability [Eq. (11)]. The $T_{\mathbf{p}}^c$ corresponds to the time it takes for the amplitude of the secondary wave \mathbf{q} (the fastest-growing perturbation of the primary wave \mathbf{p}), which has initially a small amplitude $\psi_{\mathbf{q}}(0)$, to increase by a factor $e^5 \simeq 10^2$ since the secondary waves grow as $e^{t\sigma_{\max}}$ (see the appendix). The factor of 5 that has been chosen will be justified a posteriori. We thus expect to detect the secondary waves after $5\sigma_{\max}^{-1} \simeq 150$ days. The group velocity, which determines the direction of energy propagation, is also different for the three waves (Fig. 8). It is eastward for the primary wave, westward for the long secondary wave and poleward for the short secondary wave. We thus expect to detect

the signature of the primary wave eastward of the forcing region, the signature of the long secondary wave westward of the destabilization region (which corresponds approximately to the forcing region in this case since the primary wave has a slow group velocity and the secondary wave has a fast growth rate), and the signature of the short secondary wave poleward of the forcing region.

b. Comparison with the spectral analysis of the nonlinear simulation

We perform spatial and temporal wavelet analyses of the velocity in the simulations to infer the spectral content at the time and location where we expect the primary and secondary waves to be strongest.

The primary wave is observable after a few wave periods east of the forcing region (see ray tracing in Fig. 4 and group

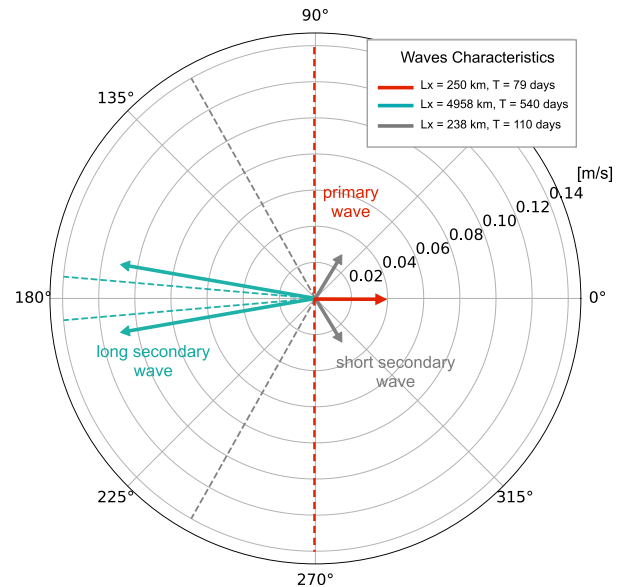


FIG. 8. Primary and secondary waves' phase lines orientation (dashed lines) and group velocity vectors (arrows) in a polar diagram; 0° represents the eastward direction, and the radial axis indicates the magnitude of the group velocity (m s^{-1}). The zonal wavelength and period of the wave are indicated in the legend.

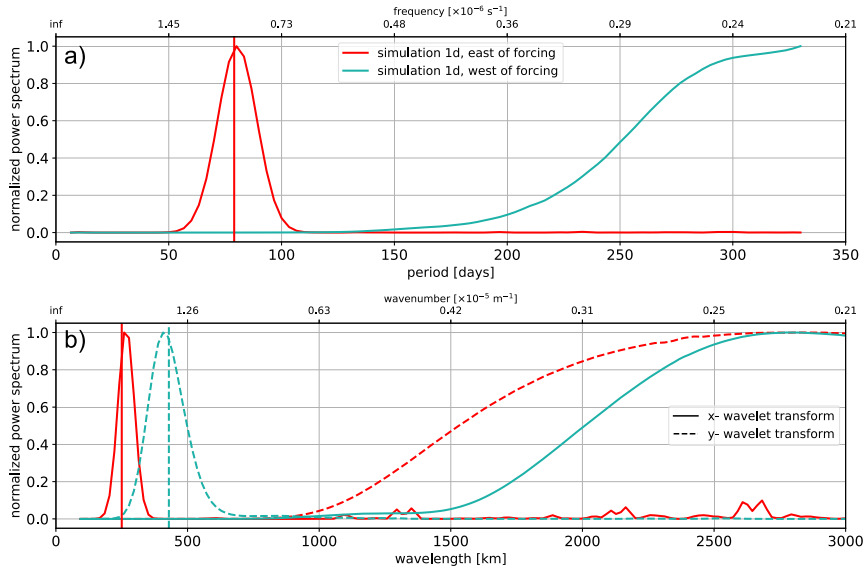


FIG. 9. (a) The time wavelet transform and (b) the space wavelet transform in the zonal direction (solid line) and in the meridional direction (dashed line). The wavelet transforms are averaged over a $2^\circ \times 2^\circ$ horizontal domain and a 20-day time interval. Vertical lines indicate the characteristics that are predicted for the primary and secondary waves (Table 2). The red curves are the spectrum of the meridional velocity at the location where the primary wave **p** is expected (red marker in Fig. 5c), and the green curves are the spectrum of the zonal velocity at the location where the long secondary wave **q** is expected (green marker in Fig. 5f).

velocity in Fig. 8). The wavelet transform in this region (red square in Fig. 5c) shows a spectral peak at a period of 79 days (Fig. 9a; solid red curve), a zonal wavelength of 250 km (Fig. 9b; solid red curve), and a long meridional wavelength of 3000 km (Fig. 9b; dashed red curve). This matches the characteristics of the expected forced primary wave (Table 2). The long secondary wave is detected west of the forcing region, the spectral characteristics measured from the wavelet transforms in this region (green square in Fig. 5f) show a long period and a long zonal wavelength [not precisely quantifiable within the spanned spectral range (Fig. 9; solid green curve)]. The meridional wavelength is around 500 km (Fig. 9b; dashed green curve). This wave has spectral characteristics consistent with the prediction from the NLTI theory (Table 2). The short secondary wave is difficult to identify in the simulations because its period and zonal wavenumber are similar to the primary wave's (Table 2). It also has a slower group velocity than the long secondary wave (Fig. 8), and its energy propagation is directed poleward, in a region where the primary wave is also present. There is thus no region where the short secondary wave can be observed alone. Its presence can, however, be identified in the two-dimensional spatial spectrum (Fig. 11c).

The time at which the instability occurs in this simulation is inferred from the wavelet scalogram, which shows the evolution of the mean spectral characteristics averaged in the basin $\overline{KE}^x(t)$, $\overline{KE}^y(t)$, and $\overline{KE}^z(t)$ (Fig. 10). The instability occurs when there is a shift in the spectral characteristics from the forced frequency and wavelengths to the emerging secondary wave, which is around $t = 275$ days in the simulation (dashed white line in Fig. 10). The shift is particularly visible for $\overline{KE}^y(t)$

(Fig. 10c) where the energy goes from a large to small meridional wavelength. The energy in the forced, small period and small zonal wavelength is concurrently strongly attenuated (Figs. 10a,b). The theoretical growth rate corresponds to an instability emergence time of ~ 150 days (section 5a). Based on Fig. 10, the spinup period, which corresponds to the time before the detection of the spectral characteristics of the primary wave, is around 130 days. The instability emergence time in the simulation (275 days) corresponds thus approximately to the sum of the spinup period and theoretical instability emergence time. The spatially averaged two-dimensional spectral kinetic energy shows that basin wide, the velocity field is dominated by the forced wave before the instability occurs (Figs. 11a,b) and by the two secondary waves after the instability occurs (Figs. 11c,d). Note that the two-dimensional spectrum \widehat{KE}^{xy} allows one to separate the contribution of the short secondary wave (Fig. 11c), and reveals that it is less energetic than the long secondary wave that is dominant in both \widehat{KE}^{xy} and \widehat{KE}^{xt} .

We have thus shown that the secondary waves that develop in the nonlinear simulations are consistent with a nonlinear triad instability. The growth rate and wavenumbers of the instability are well predicted using a nonlinear truncated theory. In the example shown, the long secondary wave has jet-like characteristics.

6. Application to the generation of jet-like structures

The objective of this section is to explore the sensitivity of the formation of jet-like long secondary waves to the

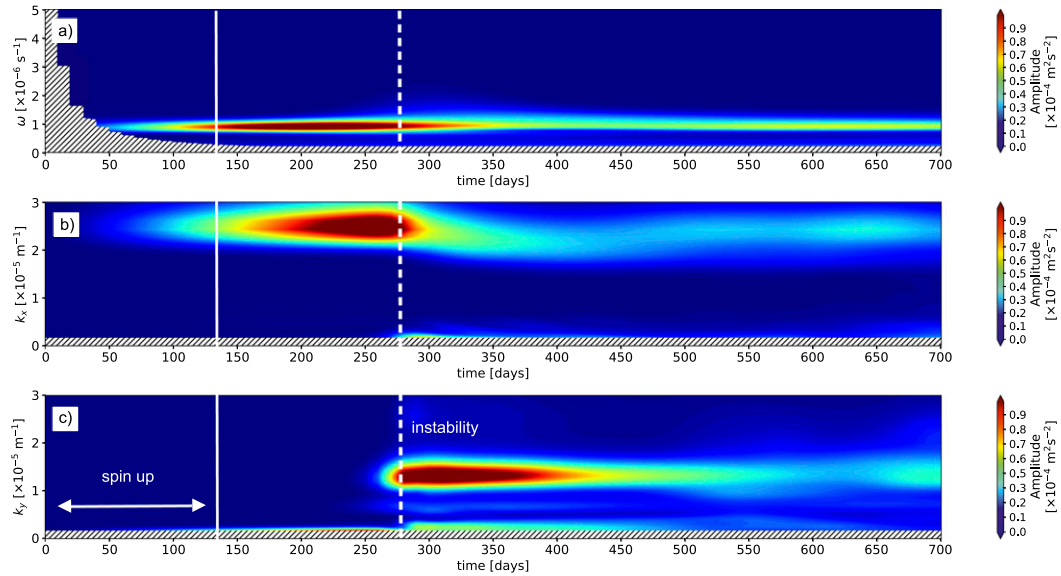


FIG. 10. Wavelet scalogram averaged in the interior of the domain (i.e., the region away from 5° of the boundary) as a function of (a) time and period \overline{KE}^t [Eq. (8)], (b) time and zonal wavenumber \overline{KE}^x , and (c) time and meridional wavenumber \overline{KE}^y . The spinup period is indicated by the arrow. The time when the instability occurs is indicated with the dashed line and corresponds to a shift in the spectra.

characteristics of the primary wave (i.e., the frequency, wavevector, and amplitude). From the simulations that have been performed, it appears that not all primary waves are able to trigger instability, nor to create waves that resemble jet-like structures.

a. Instability threshold and emergence time

Some nonlinear simulations are not subject to instability, like for example simulation 1l, in which the forced primary wave propagates without spectral modification (Figs. 5j–r). Theoretically, all primary waves are subject to triad instability (appendix). However, the growth rate can be close to zero, in which case it would take a very long time for the instability to develop, and thus it might not be realizable in numerical simulations. To determine whether a wave will be readily unstable or not, we define an instability emergence ratio [Eq. (13)] following Qiu et al. (2013), which is a combination of the instability growth rate and the primary wave energy propagation velocity. We define the instability emergence ratio as

$$R_p^e = \frac{T_p^a}{T_p^e}; \quad \text{with} \quad T_k^a = \frac{2\pi}{|\mathbf{k}| |C_{gk}|} \quad (\text{for any wave } \mathbf{k}), \quad (13)$$

where $|\mathbf{k}|$ is the modulus of the wavevector ($|\mathbf{k}| = \sqrt{k_x^2 + k_y^2}$) and $|C_{gk}|$ is the modulus of the wave group velocity vector ($|C_{gk}| = \sqrt{C_{gx}^2 + C_{gy}^2}$). Following Qiu et al. (2013), T_p^a represents the propagation time scale of the primary wave \mathbf{p} (i.e., the time needed for a wave packet to transit of one wavelength); R_p^e corresponds thus to the ratio of the propagation time scale to the instability emergence time.

The instability emergence time depends on the primary wavenumber, frequency and amplitude (Fig. 12a). As predicted

by the theoretical instability emergence ratio [Eq. (13)], simulations 1a, 1d, and 1f, should undergo triad instability (Fig. 12a). These simulations have a primary wave amplitude around 0.07 m s^{-1} (see Fig. 3b for the relation between the forcing strength and the primary wave amplitude). The emergence of the instability in these simulations is visible from the switch of spectral properties in $\overline{KE}^y(t)$ (Figs. 12b–d). In contrast, the primary wave in the simulation 1h remains stable and $\overline{KE}^y(t)$ shows a dominant meridional scale that is constant in time (Fig. 12e). This shows that the truncated NLTI theory describes well what happens in the different simulations and can be used to predict the stability or instability of the different barotropic waves in the ocean. It is interesting to note that some waves will not destabilize unless they have an unrealistic amplitude (Fig. 13). This is the case for barotropic waves with a long wavelength. For example, a wave with a tropical instability wave–like spectral signature, with a 30-day period and a 1000-km zonal wavelength destabilizes only for amplitude greater than 75 cm s^{-1} (Fig. 13). For other waves, and in particular short wavelength primary waves, the amplitude threshold needed to reach $R_p^e \geq 1$ is very low.

The time at which the instability occurs in the simulation can be approximated by the time at which the energy in the forced spectral range reaches a maximum and starts to decrease. For all unstable simulations ($R_p^e \geq 1$) this time is found to be inversely proportional to the theoretical growth rate expected from the three-mode truncation triad interaction theory (Fig. 14). Primary waves with a larger amplitude (big dots in Fig. 14) have a higher instability growth rate and thus a lower instability emergence time than primary waves with a smaller amplitude. Similarly, simulations with a higher primary wavenumber (blue dots in Fig. 14) have a higher growth rate and lower instability emergence time than simulations

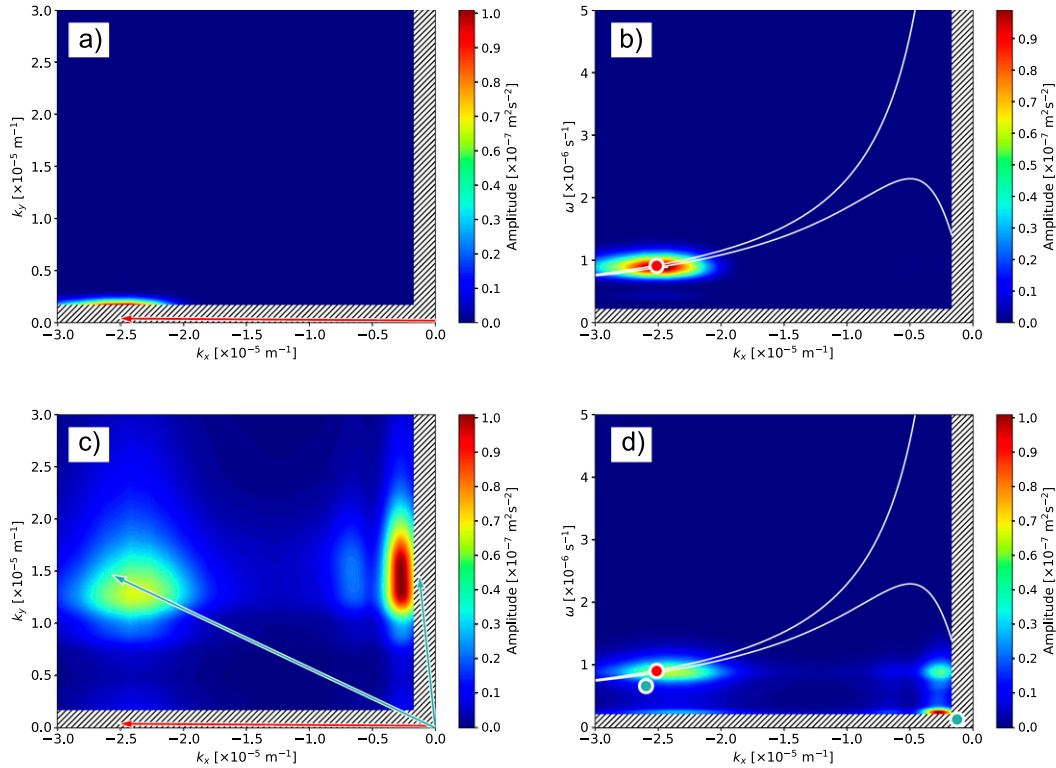


FIG. 11. Two-dimensional spectra computed from the wavelet transforms following the method described in section 3: (left) \widehat{KE}^{v_y} and (right) \widehat{KE}^{v_r} (a),(b) before the instability emerges ($t = 150$ days) and (c),(d) after the instability emerges ($t = 680$ days). The red dots and arrows indicate the theoretical frequency and wavenumbers of the primary waves. The green dots and arrows indicate the theoretical frequency and wavenumbers of the secondary waves. White curves in (b) and (d) indicate the dispersion relation for barotropic Rossby waves with $k_y = 0$ and $k_y = 2 \times 10^{-6}$.

with lower primary wavenumber (orange dots in Fig. 14). The coefficient of proportionality between the inverse of the growth rate and the emergence time is approximately equal to 5, which justifies the definition of the emergence time [Eq. (12)].

b. Selection for the secondary waves' spatial and temporal scales

The nonlinear simulations show that the secondary waves resulting from the triad instability differ from one simulation to another, for example, in their meridional wavelengths (Figs. 12b–d). The characteristics of the long secondary wave depend on the forced primary wave's wavenumbers and frequency, as inferred from the growth rate computation at a fixed amplitude (Fig. 15). The correspondence between the scale for the long secondary wave in the numerical simulations and the theoretical prediction in Fig. 15 shows that the dominant instabilities in the simulations are consistent with NLTI theory.

The long secondary wave meridional wavelength varies with the period of the primary wave ($2\pi/\omega_p$). It is shorter (~ 100 – 300 km) for long periods ($2\pi/\omega_p > 75$ days) and much longer (up to 1000 – 3000 km) for shorter periods ($2\pi/\omega_p < 50$ days). At fixed ω_p , the secondary wave meridional wavelength also

increases with decreasing p_x (Fig. 15a). The long secondary wave zonal wavelength varies nonmonotonically with along the primary wave's spectral characteristics. At fixed ω_p , it is large for short and long primary waves. It reaches a maximum for short intra-annual primary waves, with periods between 50 and 145 days, along the dispersion relation curves corresponding to low meridional wavenumbers (Fig. 15b). The long secondary wave's period is longer for short primary waves (large p_x) and shorter for long primary waves (small p_x). Similar to the zonal wavelength, the secondary wave's period reaches a maximum for short intra-annual primary waves with periods comprised between 50 and 145 days, along the dispersion relation curves for low meridional wavenumbers (Fig. 15c). The emergence time of the instability [defined by Eq. (12)] increases from about 100 days to several years from high to low p_x , respectively. Short primary waves are thus much more unstable. The short intra-annual waves described in the paragraphs above in particular have very short emergence times (Fig. 15d).

Realistic jet-like structures have a meridional wavelength of about 350 km, a long zonal wavelength (greater than 8000 km) and a long period (more than 10 years). Given the dependence of the secondary wave's properties on the primary wave's characteristics (Figs. 15a–c), the “optimal”

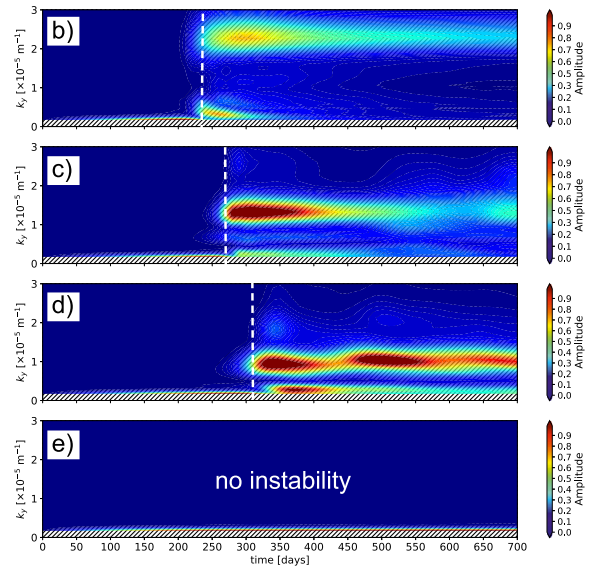
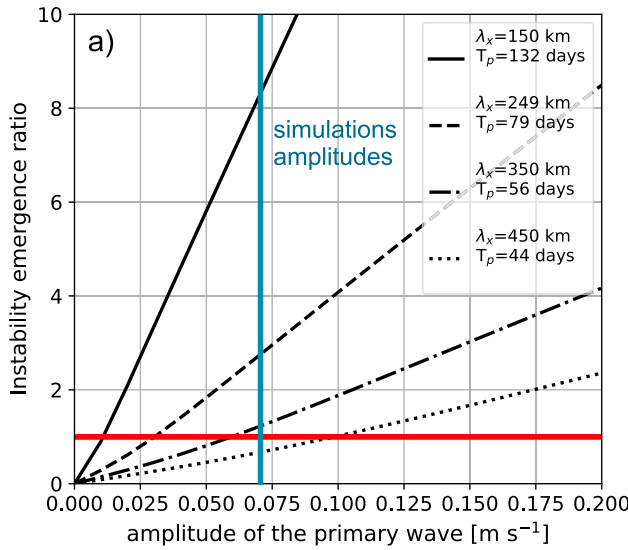


FIG. 12. (a) Theoretical instability emergence ratio as a function of the primary wave p for four waves with periods and zonal wavelengths as indicated in the legend. The instability emergence ratio [Eq. (13)] is defined as the ratio between the time it takes a wave packet to travel one wavelength and the emergence time of the secondary wave, illustrating how the instability is triggered in the simulations when this ratio exceeds 1 (i.e., for times to the right of the dashed line). Also shown is $\overline{KE}^e(t)$ for simulations (b) 1a, (c) 1d, (d) 1f, and (e) 1h.

primary waves that yield realistic jet-like secondary waves have periods between 70 and 90 days, zonal wavelengths from 200 to 300 km, and low meridional wavenumber (as indicated by the outlined box in Fig. 15). From the simulations that have been performed, simulation 1c seems to have the most realistic jet-like secondary wave. This is consistent with Fig. 6.

The analysis of the dependence of the scales of the long secondary wave to the primary wave’s properties described above

assumed a constant primary wave amplitude of 0.07 m s^{-1} , corresponding to the amplitude of the primary wave used in the numerical simulations. The optimal primary wave spectral characteristics shown in Fig. 15 are fairly robust, regardless of the primary wave’s amplitude. Indeed, Fig. 16a shows that the long secondary wave’s meridional wavelength is not very sensitive to the amplitude of the primary wave, in particular for the range of simulations that have been performed here.

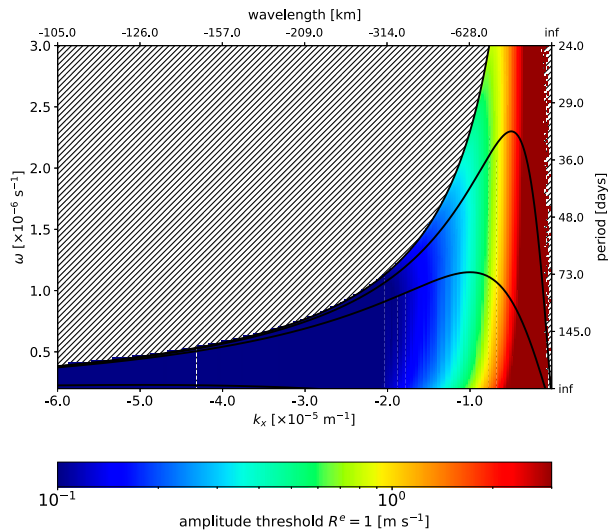


FIG. 13. Theoretical amplitude threshold to reach $R_p^e = 1$ [Eq. (13)] as a function of the primary wave zonal wavenumber k_x and frequency ω . Above this amplitude, barotropic Rossby primary waves are unstable to NLTI.

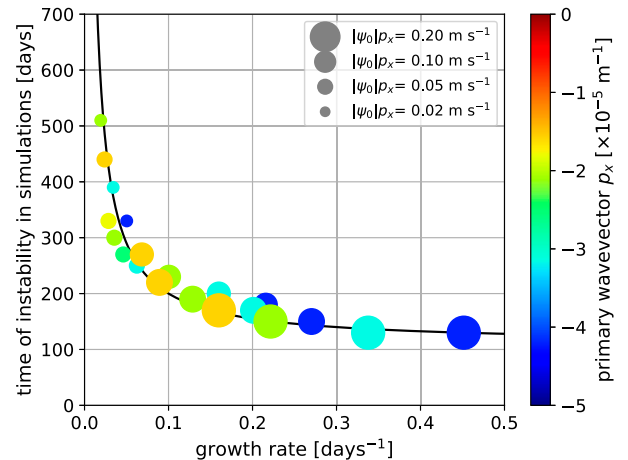


FIG. 14. The emergence time of the instability in the simulations as a function of the theoretical growth rate for the primary waves of the different simulations. Each dot represents one simulation, with size and color indicating the amplitude and zonal wavenumber of the primary wave, respectively. The black curve is proportional to the inverse of the growth rate, with a proportionality constant of 5.5.

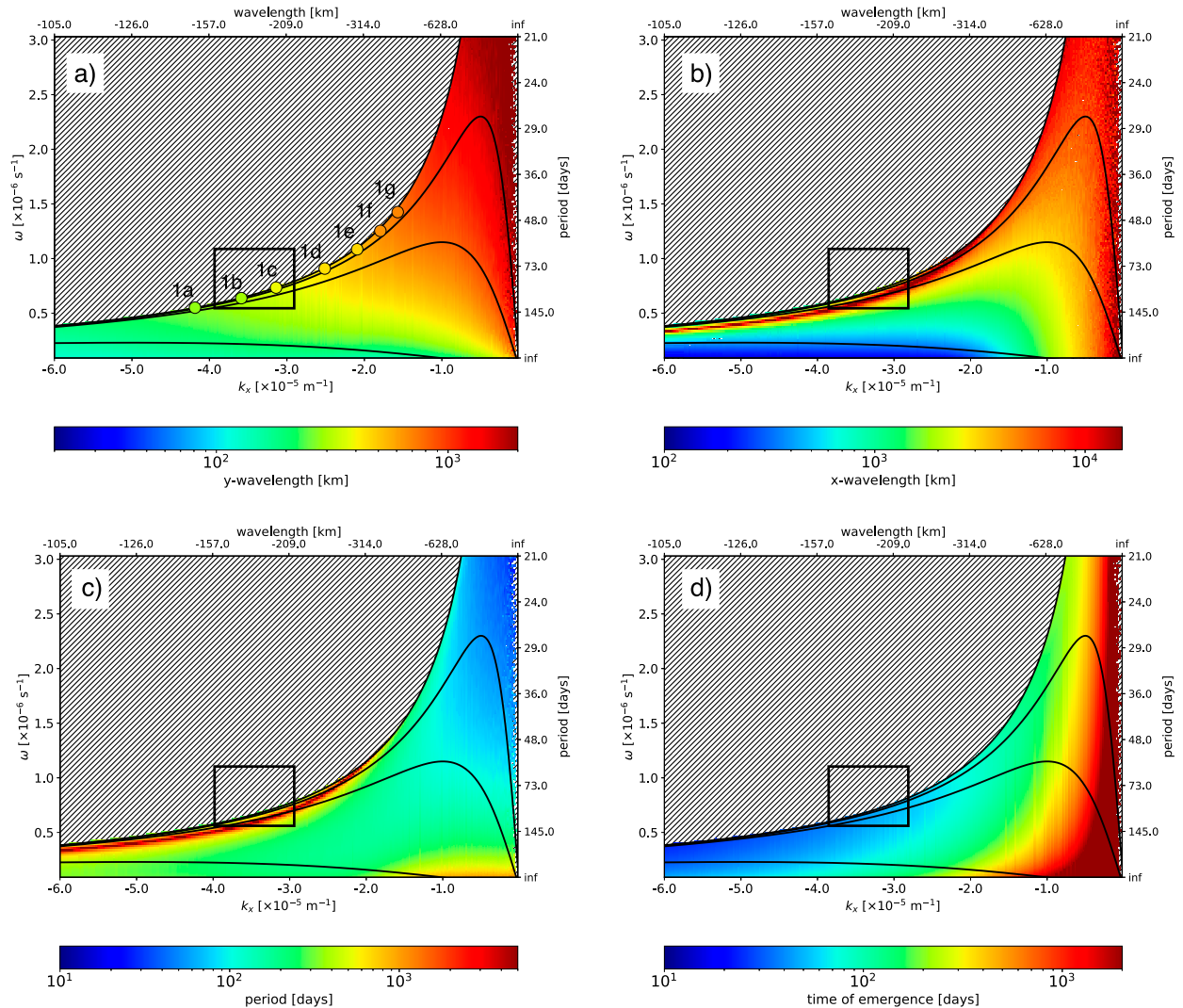


FIG. 15. Properties of the long secondary wave as a function of the primary wave’s wavelength and period with a fixed amplitude of 0.07 m s^{-1} : (a) λ_y , (b) λ_x , (c) period, and (d) time of emergence of the secondary wave. The dispersion relation for barotropic Rossby waves with different k_y is indicated by solid lines. The hatched regions correspond to regions where no instabilities grow. The black-outlined boxes are described in the text.

The variation coefficient, defined as the ratio of the standard deviation of the secondary wave’s properties across an amplitude range to the mean of these properties, is close to zero for most of the primary waves, except for waves with very high meridional wavenumbers (Fig. 16d). The secondary wave zonal wavelength varies with the amplitude of the primary wave (Figs. 16b,e). These variations, however, are not very large with respect to the values of the wavelengths: even if they vary by 1000 or 2000 kilometers, they are still long waves (i.e., with wavelengths larger than 3000 km). The variation coefficient remains less than 0.5 almost everywhere in the spectrum (Fig. 16e). The period of the long secondary wave is the most sensitive to the amplitude of the primary wave. Especially along the first barotropic dispersion relation ($k_y = 0$), where the variation coefficient is close to 0.8 (Fig. 16f) and the

secondary waves’ period can go from 200 days to a few years (Fig. 16c). In the simulations, the secondary wave meridional wavelength is also found to be not sensitive to the primary wave amplitude (Fig. 16a), illustrating again the similarity between the numerical simulations and the NLTI theory in complement of Fig. 15a.

7. Discussion, summary, and perspectives

a. Beyond the three-mode truncation theory

This study shows that NLTI theory can predict the instabilities that can form jet-like structures in the low-latitude oceans. The theoretical framework was, however, developed under strong assumptions, in particular nonlinear interactions were limited to three waves. In the model, the dynamics is

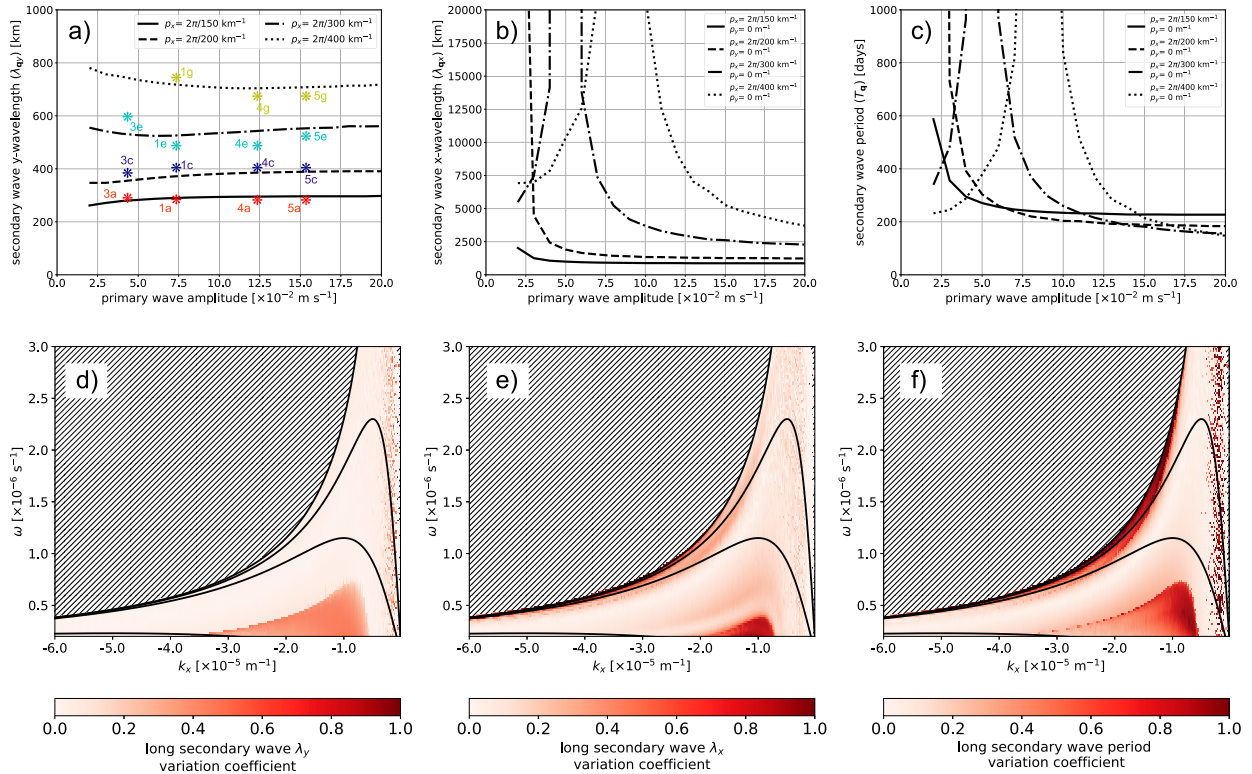


FIG. 16. Sensitivity of the long secondary waves' properties: (a) meridional wavelength λ_y , (b) zonal wavelength λ_x , (c) period, to the amplitude of the primary wave. The sensitivity is computed for primary waves with zonal wavelengths of 150, 200, 300, and 400 km and for amplitudes ranging from 0.01 to 0.3 m s^{-1} with a 0.01 m s^{-1} increment. The corresponding experiments and the secondary waves' meridional wavelengths computed using a wavelet analysis are indicated by the asterisks with their labels referring to Table 1. Also shown is the variation coefficient, namely, the ratio of the standard deviation of the properties for the different amplitude to the mean of this property, computed for (d) the secondary wave meridional wavelength λ_y , (e) zonal wavelength λ_x , and (f) period.

not truncated and the nonlinear interactions may involve additional triads of waves. However, it is interesting to note that the three-mode truncation captures the early stages of the instability process. On longer time scales, secondary instabilities may arise, which involve additional waves. The spectra show evidence of this (e.g., Fig. 11d) as they indicate that more than three waves are clearly present in the simulations. Spectral analysis of the simulation 1d on long time scales shows that

energy is present at various scales and is exchanged through a broad continuum of waves, similar to a turbulent cascade, rather than being contained in a few discrete waves (Fig. 17). Energy tends, however, to accumulate in regions where $k_x = 0$, which corresponds to jet-like structures. This might be explained by the stability of jet-like waves to NLTl. Namely, the growth rate for any jet-like primary wave, $\mathbf{p} = (0, p_y)$, is identically equal to zero (Fig. 18), such that jet-like secondary waves are very stable and will likely not undergo further triad

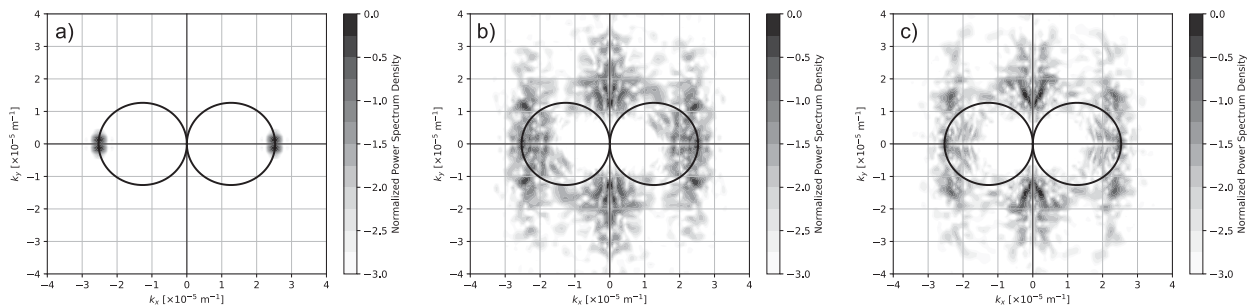


FIG. 17. Evolution of the energy spectrum in wavenumber space for simulation 1d at times (a) $t = 120$ days, (b) $t = 1000$ days, and (c) $t = 1200$ days.

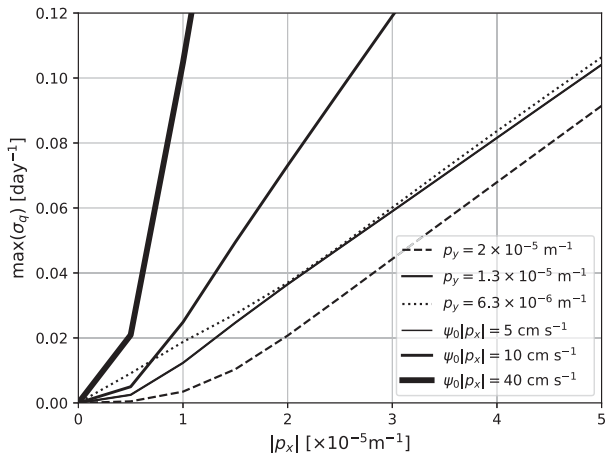


FIG. 18. The maximum growth rate [Eq. (11)] for $|p_x|$ ranging between 0 and $5 \times 10^{-5} \text{ m}^{-1}$ for different meridional primary wavenumbers p_y (line styles) and amplitude $\psi_0|p_x|$ (line widths). Jet-like waves correspond to $p_x = 0$ and always have a growth rate equal to zero, illustrating their particular stability.

interactions. The jet-like waves thus act as an attractor of this “wave cascade,” and every wave undergoing NLTI might eventually cascade toward jet-like structures. This is analogous to turbulent cascades on a beta plane, where the energy cascades from being isotropically distributed in spectral space toward accumulation zones at low frequencies and small zonal wavenumbers, which correspond to zonal jets (Rhines 1975; Vallis and Maltrud 1993).

b. Beyond barotropic dynamics

Because we are only considering a two-dimensional dynamics, we neglect the possible interactions between different vertical modes. A full description of the nonlinear dynamics of equatorial waves should consider baroclinic modes and their possible nonlinear interactions. The two-dimensional problem investigated in this paper is well posed for the barotropic mode only. Nonlinear interactions of barotropic waves indeed remain barotropic (not shown). In this case the two-dimensional reduction of the problem is a good approximation and 2D simulations are a good tool to study the NLTI. This is not the case for baroclinic waves. Nonlinear interactions of baroclinic modes project mainly on the barotropic mode (not shown). The barotropic mode thus acts also as an attractor in the wave cascade.

c. Toward a realistic mean circulation

Intra-annual waves with large wavenumbers such as the ones described in this study are not unrealistic as they have been observed in the tropical ocean (Farrar 2011; Tuchen et al. 2018; Delpech et al. 2020b). Farrar (2011) evidenced barotropic intra-annual waves in the northern tropical Pacific Ocean, radiating away from the tropical instability waves with a 30-day period and a 1000-km wavelength. Tuchen et al. (2018) described evidence of 50-day Yanai waves with a baroclinic structure at the equator. Delpech et al. (2020b) described observations of waves at 1000 m in the northern tropical Pacific

with a 70-day period and a 500-km wavelength with properties consistent with barotropic Rossby waves. It is interesting to note that the waves observed by Farrar (2011) are found to be stable to NLTI (e.g., Fig. 13). This could explain why they are seen propagating away from their generation site. On the contrary, waves unstable to NLTI have only sporadically been observed, their small wavelengths make them challenging to capture with in situ data and as they are associated with a weak signature in sea surface height (typically less than 2 cm at low latitudes), it is also difficult to capture them with the current generation Nadir altimetry. The new-generation swath satellite altimeter designed to observe submesoscale features (e.g., SWOT; Fu and Ubelmann 2014) may open new opportunities in this regard. The jet-like structures produced by the unstable intra-annual waves through NLTI are long waves with zonal wavelengths that can reach several thousands of kilometers (Fig. 16b) and with periods of several years (Fig. 16c). However, their time averaged velocities generally result in a weak mean circulation (e.g., Fig. 6a). This mechanism is therefore not sufficient to explain the observed mean deep circulation. Other mechanisms may intervene in the long term equilibration of these jet-like structures to produce the jet-structured mean circulation as has been observed in 10-yr averages of Argo float displacements (Ollitrault et al. 2006; Cravatte et al. 2012). Equilibration processes may involve modification of the potential vorticity by the zonal jets combined with positive feedback mechanisms such as eddy-driven jet sharpening (Dritschel and Scott 2011; Greatbatch et al. 2018; Ménesguen et al. 2019). In addition, the observed zonal jets are not purely barotropic and have a complex vertical structure (Qiu et al. 2013; Cravatte et al. 2017). Therefore, baroclinic dynamics could come into play and should be considered in future studies. Bottom topography could have an influence on the dynamics of barotropic Rossby waves (such as causing scattering, refraction and trapping) through the topographic beta effect (e.g., Wang and Koblinsky 1994; T. S. Durland and J. T. Farrar 2021, unpublished manuscript) and the modification of classical vertical modes (LaCasce 2017). The topographic beta effect scales as the Coriolis parameter and the bottom slope. We therefore expect it to be of lesser importance at low latitudes, away from steep continental margins or seamounts. It is, however, interesting to note that the influence of topography could transform a stable large-scale long-period Rossby wave forced by the atmosphere, into a small-scale long-period Rossby wave, subject to NLTI (Rhines and Bretherton 1973).

d. Summary and perspectives

Deep intra-annual waves, which have been frequently observed at low latitudes in the ocean are prone to instability. Focusing on the barotropic mode, we demonstrated that the energy transfer mechanism of this instability is well described by a three-mode truncation NLTI theory. The growth rate and characteristics of the instability are a function of the wave-number, frequency and amplitude of the primary wave. In particular cases, the secondary waves have jet-like structures. In this study, we showed that intra-annual waves can destabilize into jet-like structures using idealized barotropic numerical simulations of an equatorial basin forced by an oscillatory

wind stress. We determined that the primary waves that are optimal to reproduce realistic jet-like structures are intra-annual zonally propagating waves with period between 60 and 130 days, zonal wavelengths between 200 and 300 km and amplitude from 2 to 10 cm s⁻¹. The jet-like structures produced in the simulations and predicted by the theory do not capture all the properties of the time-mean deep circulation as it has been observed in low-latitude oceans (in particular, the jets are too weak). Future work should address the potential role of three-dimensional dynamics in the generation of these jets and include baroclinic modes into NLTI theory. The effects of bottom topography and variable stratification should be investigated as they can modify the properties and propagation of Rossby waves. Future work will also involve running realistic numerical simulations to study the role of NLTI and other equilibration processes in the formation of the jet-structured mean circulation within a realistic equatorial wave field.

Acknowledgments. The authors acknowledge the support of the CROCO community. CROCO is provided by <http://www.croco-ocean.org>. This work was granted access to the HPC facilities DATARMOR of the Pôle de Calcul Intensif pour la Mer at Ifremer, Brest (France). The authors are grateful to N. Ducouso and R. Benschila for their advice on the numerical code. This work benefited from fruitful discussions with C. Connaughton, E. Simmonet, B. Qiu, B. Delorme, and L. Qu. The authors are also grateful to two anonymous reviewers, whose comments helped to improve the quality of the paper. This publication is supported by the CNRS/LEFE and the CNES/TOSCA Alti-ETAO and Saral-MANCA projects.

APPENDIX

Analytical Solutions for Waves Nonlinear Triad Interactions

The aim of this section is to understand the dynamics of the forced wave and in particular its stability. We describe its stability (or instability) using a theoretical truncated nonlinear model that allows us to resolve analytically the first order of nonlinearity. We derive this problem in a quasigeostrophic framework, which corresponds to the limit of the primitive equation model for small amplitudes (a reasonable assumption when working with waves).

The two-dimensional quasigeostrophic equation for the streamfunction ψ is

$$\frac{\partial}{\partial t} (\nabla^2 \psi - F\psi) + \beta \frac{\partial \psi}{\partial x} + J(\psi, \nabla^2 \psi) = 0, \tag{A1}$$

where J is the Jacobian operator and F is the inverse of the squared deformation radius. The deformation radius is defined as $L_{R,0}$ for the barotropic deformation radius and $L_{R,n}$ for the n th baroclinic deformation radius:

$$L_{R,0} = \frac{\sqrt{gH}}{f_0}; \quad L_{R,n} = \frac{NH}{n\pi f_0}. \tag{A2}$$

A plane monochromatic wave, $\psi = \psi_0 e^{i(k_x x + k_y y - \omega t)}$, is solution of the equations if it satisfies the relation

$$\omega = \frac{-\beta k_x}{k_x^2 + k_y^2 + F}, \tag{A3}$$

which is known as the Rossby wave dispersion relation. Plane monochromatic Rossby waves are thus exact solutions of the nonlinear quasigeostrophic equation [Eq. (A1)].

However, a superposition of waves, $\psi = \sum_n \psi_n = \sum_n \psi_{0n}(t) e^{i(k_{xn}x + k_{yn}y)}$, is not an exact solution of Eq. (A1):

$$\frac{\partial}{\partial t} \left[\sum_n -(k_{xn}^2 + k_{yn}^2 + F)\psi_n \right] + \beta \sum_n i k_{xn} \psi_n + \frac{1}{2} \sum_{i,j} (k_{xi} k_{yj} - k_{xj} k_{yi})(k_i^2 - k_j^2) \psi_i \psi_j = 0. \tag{A4}$$

Because of the quadratic nature of nonlinear Jacobian term in Eq. (A1), the waves interaction is triadic: the waves i, j , and n interact together and their amplitude ψ_0 depend on time.

The equation for the evolution of a wave of streamfunction $\psi_{\mathbf{k}}$ and wavenumber \mathbf{k} is then given by

$$\frac{\partial}{\partial t} \psi_{\mathbf{k}} + i\omega_{\mathbf{k}} \psi_{\mathbf{k}} + \frac{1}{2} \sum_{2_{i,j}|\mathbf{k}_i+\mathbf{k}_j=\mathbf{k}} T(\mathbf{k}, \mathbf{k}_i, \mathbf{k}_j) \psi_{\mathbf{k}_i} \psi_{\mathbf{k}_j} = 0, \tag{A5}$$

where

$$\omega_{\mathbf{k}} = -\frac{\beta k_x}{k_x^2 + k_y^2 + F}; \quad T(\mathbf{k}, \mathbf{k}_i, \mathbf{k}_j) = -\frac{(\mathbf{k}_i \times \mathbf{k}_j)_z (k_i^2 - k_j^2)}{k^2 + F}, \tag{A6}$$

where T is the triadic interaction term.

For simplicity and to keep the problem analytically solvable, we consider in a first time a reduced problem for which only one triad (three waves) is retained. We note \mathbf{p}, \mathbf{q} , and $\mathbf{p} - \mathbf{q}$ as the wavevectors of these three waves, such that $\mathbf{p} = \mathbf{q} + \mathbf{p} - \mathbf{q}$. Following Eq. (A5), we can derive an equation for each of these waves:

$$\begin{cases} \partial_t \psi_{0\mathbf{p}} + i\omega_{\mathbf{p}} \psi_{0\mathbf{p}} + T(\mathbf{p}, \mathbf{q}, \mathbf{p}-) \psi_{0\mathbf{q}} \psi_{0\mathbf{p}-} = 0 \\ \partial_t \psi_{0\mathbf{q}} + i\omega_{\mathbf{q}} \psi_{0\mathbf{q}} + T(\mathbf{q}, \mathbf{p}, \mathbf{p}-) \psi_{0\mathbf{p}} \psi_{0\mathbf{p}-}^* = 0 \\ \partial_t \psi_{0\mathbf{p}-} + i\omega_{\mathbf{p}-} \psi_{0\mathbf{p}-} + T(\mathbf{p}-, \mathbf{p}, -\mathbf{q}) \psi_{0\mathbf{p}} \psi_{0\mathbf{q}}^* = 0 \end{cases}, \tag{A7}$$

where the asterisk denotes the conjugate of a complex. $\psi_{0\mathbf{k}}^* = \psi_{0-\mathbf{k}}$. Introducing $\psi_{\mathbf{k}}(t) = \psi_{0\mathbf{k}}(t) e^{-i\omega_{\mathbf{k}} t}$ Eq. (A7) becomes

$$\begin{cases} \partial_t \psi_{\mathbf{p}} + T(\mathbf{p}, \mathbf{q}, \mathbf{p}-) \psi_{\mathbf{q}} \psi_{\mathbf{p}-} e^{i\Delta t} = 0 \\ \partial_t \psi_{\mathbf{q}} + T(\mathbf{q}, \mathbf{p}, \mathbf{p}-) \psi_{\mathbf{p}} \psi_{\mathbf{p}-}^* e^{-i\Delta t} = 0 \\ \partial_t \psi_{\mathbf{p}-} + T(\mathbf{p}-, \mathbf{p}, -\mathbf{q}) \psi_{\mathbf{p}} \psi_{\mathbf{q}}^* e^{-i\Delta t} = 0 \end{cases}, \tag{A8}$$

where $\Delta = \omega_{\mathbf{p}} - \omega_{\mathbf{q}} - \omega_{\mathbf{p}-}$.

The process we want to study in the framework of our numerical simulations is the instability of a primary wave of wavevector \mathbf{p} . We linearize Eq. (A8) around the basic state $\psi_{\mathbf{p}}$, with the perturbations $\psi_{\mathbf{q}}$ and $\psi_{\mathbf{p}-}$:

$$\begin{cases} \partial_t \tilde{\psi}_{\mathbf{q}} + T(\mathbf{q}, \mathbf{p}, -\mathbf{p}_-) \psi_{\mathbf{p}} \tilde{\psi}_{\mathbf{p}_-}^* e^{-i\Delta t} = 0 \\ \partial_t \tilde{\psi}_{\mathbf{p}_-}^* + T(\mathbf{p}_-, \mathbf{p}, -\mathbf{q}) \psi_{\mathbf{p}}^* \tilde{\psi}_{\mathbf{q}} e^{i\Delta t} = 0 \end{cases} \quad (\text{A9})$$

Solutions of these equations are harmonics:

$$\begin{cases} \tilde{\psi}_{\mathbf{q}}(t) = A_{\mathbf{q}} e^{-i\sigma_{\mathbf{q}} t} \\ \tilde{\psi}_{\mathbf{p}_-}^*(t) = A_{\mathbf{p}_-}^* e^{-i\sigma_{\mathbf{p}_-} t} \end{cases} \quad (\text{A10})$$

The instability occurs if $\text{Im}(\sigma_{\mathbf{q}}) > 0$ and $\text{Im}(\sigma_{\mathbf{p}_-}) > 0$; $\text{Im}(\sigma)$ is the growth rate of the instability. The secondary waves \mathbf{q} and \mathbf{p}_- are determined as the waves that give the maximum growth rate of instability.

The linear system in Eq. (A9) then becomes, using $\sigma_{\mathbf{q}} + \sigma_{\mathbf{p}_-}^* - \Delta = 0$,

$$\begin{bmatrix} -i\sigma_{\mathbf{q}} & T(\mathbf{q}, \mathbf{p}, -\mathbf{p}_-) \psi_{\mathbf{p}} \\ T(\mathbf{p}_-, \mathbf{p}, -\mathbf{q}) \psi_{\mathbf{p}}^* & i\sigma_{\mathbf{p}_-}^* \end{bmatrix} \begin{pmatrix} A_{\mathbf{q}} \\ A_{\mathbf{p}_-}^* \end{pmatrix} = 0. \quad (\text{A11})$$

Nontrivial solutions exist if the determinant of the matrix is equal to 0:

$$\sigma_{\mathbf{q}}^2 - \Delta \sigma_{\mathbf{q}} + T(\mathbf{q}, \mathbf{p}, -\mathbf{p}_-) T(\mathbf{p}_-, \mathbf{p}, -\mathbf{q}) |\psi_{\mathbf{p}}|^2 = 0, \quad (\text{A12})$$

which gives solutions for the growth rate

$$\sigma_{\mathbf{q}} = \frac{1}{2} \left[\Delta \pm \sqrt{\Delta^2 - 4 |\psi_{\mathbf{p}}|^2 T(\mathbf{q}, \mathbf{p}, -\mathbf{p}_-) T(\mathbf{p}_-, \mathbf{p}, -\mathbf{q})} \right]. \quad (\text{A13})$$

Note that the two secondary waves \mathbf{q} and \mathbf{p}_- have the same growth rate as $\text{Im}(\sigma_{\mathbf{q}}) = \text{Im}(\sigma_{\mathbf{p}_-})$.

REFERENCES

Ascani, F., E. Firing, P. Dutriex, J. P. McCreary, and A. Ishida, 2010: Deep equatorial ocean circulation induced by a forced-dissipated Yanai beam. *J. Phys. Oceanogr.*, **40**, 1118–1142, <https://doi.org/10.1175/2010JPO4356.1>.

Bunge, L., C. Provost, B. L. Hua, and A. Kartavtseff, 2008: Variability at intermediate depths at the equator in the Atlantic Ocean in 2000–06: Annual cycle, equatorial deep jets, and intraseasonal meridional velocity fluctuations. *J. Phys. Oceanogr.*, **38**, 1794–1806, <https://doi.org/10.1175/2008JPO3781.1>.

Connaughton, C. P., B. T. Nadiga, S. V. Nazarenko, and B. E. Quinn, 2010: Modulational instability of Rossby and drift waves and generation of zonal jets. *J. Fluid Mech.*, **654**, 207–231, <https://doi.org/10.1017/S0022112010000510>.

Cox, M. D., 1980: Generation and propagation of 30-day waves in a numerical model of the Pacific. *J. Phys. Oceanogr.*, **10**, 1168–1186, [https://doi.org/10.1175/1520-0485\(1980\)010<1168:GAPODW>2.0.CO;2](https://doi.org/10.1175/1520-0485(1980)010<1168:GAPODW>2.0.CO;2).

Cravatte, S., W. S. Kessler, and F. Marin, 2012: Intermediate zonal jets in the tropical Pacific Ocean observed by Argo floats. *J. Phys. Oceanogr.*, **42**, 1475–1485, <https://doi.org/10.1175/JPO-D-11-0206.1>.

—, E. Kestenare, F. Marin, P. Dutriex, and E. Firing, 2017: Subthermocline and intermediate zonal currents in the tropical Pacific Ocean: Paths and vertical structure. *J. Phys. Oceanogr.*, **47**, 2305–2324, <https://doi.org/10.1175/JPO-D-17-0043.1>.

Delpech, A., S. Cravatte, F. Marin, Y. Morel, E. Gronchi, and E. Kestenare, 2020a: Observed tracer fields structuration

by middepth zonal jets in the tropical Pacific. *J. Phys. Oceanogr.*, **50**, 281–304, <https://doi.org/10.1175/JPO-D-19-0132.1>.

—, —, —, —, and C. Menesguen, 2020b: Deep eddy kinetic energy in the tropical pacific from Lagrangian floats. *J. Geophys. Res. Oceans*, **125**, e2020JC016313, <https://doi.org/10.1029/2020JC016313>.

d’Orgeville, M., B. L. Hua, and H. Sasaki, 2007: Equatorial deep jets triggered by a large vertical scale variability within the western boundary layer. *J. Mar. Res.*, **65**, 1–25, <https://doi.org/10.1357/002224007780388720>.

Dritschel, D., and R. Scott, 2011: Jet sharpening by turbulent mixing. *Philos. Trans. Roy. Soc. London*, **369A**, 754–770, <https://doi.org/10.1098/rsta.2010.0306>.

Eriksen, C. C., and J. G. Richman, 1988: An estimate of equatorial wave energy flux at 9- to 90-day periods in the central Pacific. *J. Geophys. Res.*, **93**, 15 455–15 466, <https://doi.org/10.1029/JC093iC12p15455>.

Farrar, J. T., 2011: Barotropic Rossby waves radiating from tropical instability waves in the Pacific Ocean. *J. Phys. Oceanogr.*, **41**, 1160–1181, <https://doi.org/10.1175/2011JPO4547.1>.

—, and R. A. Weller, 2006: Intraseasonal variability near 10°N in the eastern tropical Pacific Ocean. *J. Geophys. Res.*, **111**, C05015, <https://doi.org/10.1029/2005JC002989>.

—, and T. S. Durland, 2012: Wavenumber–frequency spectra of inertia–gravity and mixed Rossby–gravity waves in the equatorial Pacific Ocean. *J. Phys. Oceanogr.*, **42**, 1859–1881, <https://doi.org/10.1175/JPO-D-11-0235.1>.

Firing, E., 1987: Deep zonal currents in the central equatorial Pacific. *J. Mar. Res.*, **45**, 791–812, <https://doi.org/10.1357/002224087788327163>.

—, S. E. Wijffels, and P. Hacker, 1998: Equatorial subthermocline currents across the pacific. *J. Geophys. Res.*, **103**, 21 413–21 423, <https://doi.org/10.1029/98JC01944>.

Fu, L.-L., and C. Ubelmann, 2014: On the transition from profile altimeter to swath altimeter for observing global ocean surface topography. *J. Atmos. Oceanic Technol.*, **31**, 560–568, <https://doi.org/10.1175/JTECH-D-13-00109.1>.

Gargour, C., M. Gabrea, V. Ramachandran, and J.-M. Lina, 2009: A short introduction to wavelets and their applications. *IEEE Circuits Syst. Mag.*, **9**, 57–68, <https://doi.org/10.1109/MCAS.2009.932556>.

Gill, A., 1974: The stability of planetary waves on an infinite beta-plane. *Geophys. Astrophys. Fluid Dyn.*, **6**, 29–47, <https://doi.org/10.1080/03091927409365786>.

Graps, A., 1995: An introduction to wavelets. *IEEE Comput. Sci. Eng.*, **2**, 50–61, <https://doi.org/10.1109/99.388960>.

Greatbatch, R. J., and Coauthors, 2018: Evidence for the maintenance of slowly varying equatorial currents by intraseasonal variability. *Geophys. Res. Lett.*, **45**, 1923–1929, <https://doi.org/10.1002/2017GL076662>.

Hua, B. L., M. D’Orgeville, M. D. Fruman, C. Menesguen, R. Schopp, P. Klein, and H. Sasaki, 2008: Destabilization of mixed Rossby gravity waves and the formation of equatorial zonal jets. *J. Fluid Mech.*, **610**, 311–341, <https://doi.org/10.1017/S0022112008002656>.

Johnson, G. C., E. Kunze, K. E. McTaggart, and D. W. Moore, 2002: Temporal and spatial structure of the equatorial deep jets in the Pacific Ocean. *J. Phys. Oceanogr.*, **32**, 3396–3407, [https://doi.org/10.1175/1520-0485\(2002\)032<3396:TASSOT>2.0.CO;2](https://doi.org/10.1175/1520-0485(2002)032<3396:TASSOT>2.0.CO;2).

Kessler, W. S., and J. P. McCreary, 1993: The annual wind-driven Rossby wave in the subthermocline equatorial pacific.

- J. Phys. Oceanogr.*, **23**, 1192–1207, [https://doi.org/10.1175/1520-0485\(1993\)023<1192:TAWDRW>2.0.CO;2](https://doi.org/10.1175/1520-0485(1993)023<1192:TAWDRW>2.0.CO;2).
- LaCasce, J. H., 2017: The prevalence of oceanic surface modes. *Geophys. Res. Lett.*, **44**, 11–097, <https://doi.org/10.1002/2017GL075430>.
- Lebedev, K. V., H. Yoshinari, N. A. Maximenko, and P. W. Hacker, 2007: Velocity data assessed from trajectories of Argo floats at parking level and at the sea surface. IPRC Tech. Note 4(2), 20 pp., <http://apdrc.soest.hawaii.edu/projects/Argo/data/Documentation/YoMaHa070612.pdf>.
- Lee, G., R. Gommers, F. Waselewski, K. Wohlfahrt, and A. O’Leary, 2019: Pywavelets: A Python package for wavelet analysis. *J. Open Source Software*, **4**, 1237, <https://doi.org/10.21105/joss.01237>.
- Lee, T., T. Farrar, S. Arnault, B. Meyssignac, W. Han, and T. Durland, 2017: Monitoring and interpreting the tropical oceans by satellite altimetry. *Satellite Altimetry Over Oceans and Land Surfaces*, D. Stammer and A. Cazenave, Eds., CRC Press, chapter 7, 40 pp., <https://doi.org/10.1201/9781315151779>.
- Lyman, J. M., D. B. Chelton, R. A. DeSzoeke, and R. M. Samelson, 2005: Tropical instability waves as a resonance between equatorial Rossby waves. *J. Phys. Oceanogr.*, **35**, 232–254, <https://doi.org/10.1175/JPO-2668.1>.
- , G. C. Johnson, and W. S. Kessler, 2007: Distinct 17- and 33-day tropical instability waves in subsurface observations. *J. Phys. Oceanogr.*, **37**, 855–872, <https://doi.org/10.1175/JPO3023.1>.
- Maximenko, N. A., B. Bang, and H. Sasaki, 2005: Observational evidence of alternating zonal jets in the world ocean. *Geophys. Res. Lett.*, **32**, L12607, <https://doi.org/10.1029/2005GL022728>.
- Ménesguen, C., B. L. Hua, M. D. Fruman, and R. Schopp, 2009: Dynamics of the combined extra-equatorial and equatorial deep jets in the Atlantic. *J. Mar. Res.*, **67**, 323–346, <https://doi.org/10.1357/002224009789954766>.
- , A. Delpech, F. Marin, S. Cravatte, R. Schopp, and Y. Morel, 2019: Observations and mechanisms for the formation of deep equatorial and tropical circulation. *Earth Space Sci.*, **6**, 370–386, <https://doi.org/10.1029/2018EA000438>.
- Ollitrault, M., and A. Colin de Verdière, 2014: The ocean general circulation near 1000-m depth. *J. Phys. Oceanogr.*, **44**, 384–409, <https://doi.org/10.1175/JPO-D-13-030.1>.
- , M. Lankhorst, D. Fratantoni, P. Richardson, and W. Zenk, 2006: Zonal intermediate currents in the equatorial Atlantic Ocean. *Geophys. Res. Lett.*, **33**, L05605, <https://doi.org/10.1029/2005GL025368>.
- Pedlosky, J., 2013: *Geophysical Fluid Dynamics*. Springer Science & Business Media, 710 pp.
- Qiu, B., S. Chen, and H. Sasaki, 2013: Generation of the north equatorial undercurrent jets by triad baroclinic Rossby wave interactions. *J. Phys. Oceanogr.*, **43**, 2682–2698, <https://doi.org/10.1175/JPO-D-13-099.1>.
- Rhines, P. B., 1975: Waves and turbulence on a beta-plane. *J. Fluid Mech.*, **69**, 417–443, <https://doi.org/10.1017/S0022112075001504>.
- , and F. Bretherton, 1973: Topographic Rossby waves in a rough-bottomed ocean. *J. Fluid Mech.*, **61**, 583–607, <https://doi.org/10.1017/S002211207300087X>.
- Rohith, B., A. Paul, F. Durand, L. Testut, S. Prerna, M. Afroosa, S. Ramakrishna, and S. Shenoi, 2019: Basin-wide sea level coherency in the tropical Indian Ocean driven by Madden-Julian oscillation. *Nat. Commun.*, **10**, 1257, <https://doi.org/10.1038/s41467-019-09243-5>.
- Schopf, P. S., D. L. Anderson, and R. Smith, 1981: Beta-dispersion of low-frequency Rossby waves. *Dyn. Atmos. Oceans*, **5**, 187–214, [https://doi.org/10.1016/0377-0265\(81\)90011-7](https://doi.org/10.1016/0377-0265(81)90011-7).
- Shchepetkin, A. F., and J. J. O’Brien, 1996: A physically consistent formulation of lateral friction in shallow-water equation ocean models. *Mon. Wea. Rev.*, **124**, 1285–1300, [https://doi.org/10.1175/1520-0493\(1996\)124<1285:APCFOL>2.0.CO;2](https://doi.org/10.1175/1520-0493(1996)124<1285:APCFOL>2.0.CO;2).
- , and J. C. McWilliams, 2005: The Regional Oceanic Modeling System (ROMS): A split-explicit, free-surface, topography-following-coordinate oceanic model. *Ocean Modell.*, **9**, 347–404, <https://doi.org/10.1016/j.ocemod.2004.08.002>.
- , and —, 2009: Computational kernel algorithms for fine-scale, multiprocess, longtime oceanic simulations. *Special Volume: Computational Methods for the Atmosphere and the Oceans*, R. M. Temam and J. J. Tribbia, Eds., Vol. 14, Handbook of Numerical Analysis, Elsevier, 121–183, [https://doi.org/10.1016/S1570-8659\(08\)01202-0](https://doi.org/10.1016/S1570-8659(08)01202-0).
- Torrence, C., and G. P. Compo, 1998: A practical guide to wavelet analysis. *Bull. Amer. Meteor. Soc.*, **79**, 61–78, [https://doi.org/10.1175/1520-0477\(1998\)079<0061:APGTWA>2.0.CO;2](https://doi.org/10.1175/1520-0477(1998)079<0061:APGTWA>2.0.CO;2).
- Tuchen, F. P., P. Brandt, M. Claus, and R. Hummels, 2018: Deep intraseasonal variability in the central equatorial Atlantic. *J. Phys. Oceanogr.*, **48**, 2851–2865, <https://doi.org/10.1175/JPO-D-18-0059.1>.
- Vallis, G. K., and M. E. Maltrud, 1993: Generation of mean flows and jets on a beta plane and over topography. *J. Phys. Oceanogr.*, **23**, 1346–1362, [https://doi.org/10.1175/1520-0485\(1993\)023<1346:GOMFAJ>2.0.CO;2](https://doi.org/10.1175/1520-0485(1993)023<1346:GOMFAJ>2.0.CO;2).
- von Schuckmann, K., P. Brandt, and C. Eden, 2008: Generation of tropical instability waves in the Atlantic Ocean. *J. Geophys. Res.*, **113**, C08034, <https://doi.org/10.1029/2007JC004712>.
- Wang, L., and C. J. Kobalinsky, 1994: Influence of mid-ocean ridges on Rossby waves. *J. Geophys. Res.*, **99**, 25 143–25 153, <https://doi.org/10.1029/94JC02374>.